Deposition and Corrosion Performance of Phosphate-Polylactic Acid Composite Coatings on WE43 Magnesium Alloy

Andrei V. Paspelau[a,b,*], Aliaksandr A. Kasach[c], Jacek Gurgul[d], Grzegorz Mordarski[e,f], Konrad Skowron[e,f], Irina I. Kurilo[b], and Dzmitry S. Kharytonau[e,f,*]

[a]Centre for Physical and Chemical Investigation Methods, Belarusian State Technological University, 220006 Minsk, Belarus

[b]Department of Physical, Colloid, and Analytical Chemistry, Belarusian State Technological University, 220006 Minsk, Belarus

[c]Department of Chemistry, Electrochemical Production Technology, and Materials for Electronic Equipment, Belarusian State Technological University, 220006 Minsk, Belarus

[d]Surface Nanostructures, Jerzy Haber Institute of Catalysis and Surface Chemistry, Polish Academy of Sciences, 30-239 Krakow, Poland

[e]Electrochemistry and Corrosion Laboratory, Jerzy Haber Institute of Catalysis and Surface Chemistry, Polish Academy of Sciences, 30-239 Krakow, Poland

[f]Soft Matter Nanostructures, Jerzy Haber Institute of Catalysis and Surface Chemistry, Polish Academy of Sciences, 30-239 Krakow, Poland

[*]Corresponding authors:

Andrei V. Paspelau: andrei29088@mail.ru; Centre for Physical and Chemical Investigation Methods, Belarusian State Technological University

Dzmitry S. Kharytonau: dmitry.kharitonov@ikifp.edu.pl; Jerzy Haber Institute of Catalysis and Surface Chemistry, Polish Academy of Sciences. ORCID: 0000-0003-2071-3975;

Abstract

The degradation profile of Mg alloys in biomedical environments can be controlled by applying various types of surface coatings. Phosphate chemical conversion coatings (CaP) and polylactic acid (PLA) biopolymer coatings are biocompatible and promising for the corrosion protection of Mg alloys. The aim of this work was to investigate the physicochemical properties and corrosion performance of inorganic, organic, and mixed inorganic-organic coatings. Three types of surface modification, CaP, PLA, and a combined CaP-PLA coating were obtained on the surface of the magnesium alloy WE43. Scanning electron microscopy, X-ray diffraction, X-ray photoelectron spectroscopy, and infrared spectroscopy were employed to characterize the surface and interfacial morphology, along with the composition of the coatings before and after corrosion experiments. The protective performance of obtained coatings was examined by electrochemical impedance spectroscopy and immersion testing in Hank's solution. The results allowed to propose the mechanism of the coatings growth and their further corrosion degradation. A two-component CaP-PLA coating provided reliable corrosion resistance in Hank's solution for 14 days.

Keywords: Magnesium alloy; Polylactic Acid; Calcium Hydrogen Phosphate; Corrosion Mechanism, Hank's Solution

1. Introduction

The development of reliable metallic implant materials designed to replace bone tissue and fix bone fractures gained immense scientific and practical interest. Such materials should combine biological compatibility with human organisms and mechanical properties similar to those of native bone tissue [1]. Modern metallic implants include commercially pure titanium, Ti-6Al-4V alloy, 316L stainless steel, and cobalt-chromium alloys [2,3]. Due to the discrepancy between the mechanical properties of a natural bone (Young's modulus 10–30 GPa) and implant materials (Young's modulus 100–200 GPa) [4,5], the latter has a serious drawback called stress shielding [6]. Insufficient load on healthy bone tissue leads to its resorption and loosening of the implant, reducing its life. In addition, after bone healing, metal implants usually need to be removed within two years of the first surgery [7,8], with medical, social, and economic consequences and costs [9].

Another concept of biomedical materials includes biodegradable metallic implants. The development and implementation of biodegradable implants is a promising way to eliminate the problem of repeated surgical interventions [10–12]. In particular, magnesium is one of the best materials for the manufacture of biodegradable implants. Biodegradation of Mg proceeds with hydrogen depolarization and can lead to a violation of the mechanical integrity of the implant before the bone heals. The main approaches to reduce the rate of biodegradation of Mg are alloying and surface functionalization. Alloying with Zn, Ca, and Y significantly improves the mechanical properties of Mg [13–16]. These elements also improve the corrosion resistance of magnesium and, accordingly, reduce the rate of hydrogen evolution [17,18]. The Mg alloy WE43 is a high-strength Mg alloy with Y and Nd as the main alloying elements. It has high creep resistance and biocompatibility, suitable mechanical properties, and density close to those of native bone [19–22]. Importantly, its corrosion products are nontoxic, and it does not contain Al, which is considered to be neurotoxic and can cause dementia and Alzheimer’s disease [23,24].

The main drawback of Mg-based materials is their rapid corrosion in biological media [21,25,26]. Surface modification of Mg and its alloys is widely used to form functional coatings for various purposes [21,25,27]. Conversion treatment is the most accessible and simple method of the surface modification of metals [21,25,28]. In terms of biomedical applications, the most common conversion coatings include phosphates, rare earth, Al-Mg layered double hydroxides, and some organic polymers [27].

Phosphate chemical conversion treatment is a process in which a protective film is obtained by the reaction of the Mg substrate with phosphating agents in the bath. To tune the coating properties according to the target applications, the deposition bath is usually modified by adding different cations [27,29]. In this manner it is possible to obtain coatings based on calcium phosphates (CaP), which have high chemical resistance in biological media and excellent biocompatibility and are osteoconductive and bioresorbable [27,30,31]. It is known [32,33], that CaP conversion layers can reduce the corrosion rate of magnesium alloys by almost 10 times. However, CaP layers formed on the surface of magnesium alloys often have inhomogeneous morphology with many cracks and pores [34]. These pores originate from the release of hydrogen bubbles from the magnesium substrate with the formation of a CaP layer around them.

Organic coatings provide more flexibility in terms of chemical functionalization of the metal surface to mimic the multi-functional performance of the natural bone [35]. As organic coatings on magnesium alloys, various biopolymers are used [35–39], whose mechanical properties are comparable to those of soft biological tissues. In addition, polymer coatings can be modified by multifunctional inhibitors or drug carriers [35,40],

Recently, biocompatible and bioresorbable polymers, such as polylactic acid (PLA) has been extensively examined as a promising tool to modify biodegradable Mg-based materials [35]. It has been shown [38,41] that PLA coatings reduce the corrosion rate of magnesium and its alloys in biological media. The deposition of a multilayer PLA coating on the AZ31 magnesium alloy led to an increase in the polarization resistance R_p by almost 3.5 times. It has also been reported

[42], that the use of PLA to modify the magnesium surface significantly improves cytocompatibility and reduces the release of Mg^{2+} ions during cell culture tests, which indicates an increase in the corrosion resistance of the magnesium substrate.

Compared to single polymer layers, multilayer coatings consisting of inorganic and organic layers showed higher anticorrosion efficiency [35,40,43–45]. Biopolymer supports cell growth, biocompatibility, and controlled biodegradation, while the inorganic layer improves the mechanical properties of the material (Young's modulus, compressive strength), bioactivity, and osseointegration [46,47]. The combination of organic and inorganic layers makes it possible to create new multifunctional materials for bioengineering.

Effectiveness of the corrosion protection of Mg alloys highly depends on their microstructure and alloying elements [27,48–50]. In the case of conversion coatings, the composition of the used substrate also plays an important role in the process of the coating formation and its further corrosion performance [27,51]. To date, most studies on the development of conversion coatings have been devoted to the AZ-series (Mg-Al-Zn) alloys [27,52], while the information on the protection of the Mg-rare earth alloys, like WE43, is very limited. In most cases, corrosion properties of the formed layers are evaluated in NaCl solutions and, less often, in SBF solution [27,52]. However, the WE43 alloy is a promising candidate for biomedical applications and examination of its corrosion in different biologically relevant media is of great importance [53,54]. In our recent study [26] we have shown a significant difference in corrosion mechanisms between the AZ31 and WE43 alloys in Hank’s solution, with a more complex mechanism involved in corrosion of the WE43 alloy. Based on this, the formation of the protective coatings on the surface of the WE43 alloy and their corrosion resistance should also be examined. The aim of this work was to investigate the physicochemical properties and corrosion performance of inorganic, organic, and mixed inorganic-organic coatings on the surface of the WE43 alloy in Hank’s solution and evaluate their corrosion mechanisms. Three types of coatings, a conventional phosphate conversion coating (CaP), an organic PLA coating, and a combined CaP-PLA coating

were obtained on the surface of the magnesium alloy WE43. The properties of as-treated samples were comparatively investigated in Hank's solution through immersion and electrochemical impedance spectroscopy (EIS) tests. Special attention has been paid to the spectroscopic examination of the coatings after long-term exposure to Hank's solution, which is rarely reported in the literature but is important in the understanding of their degradation profile.

2. Experimental

2.1. Materials and sample preparation

The magnesium alloy WE43 containing rare-earth elements was used in this study. The alloy was obtained according to the procedure reported elsewhere [50]. The chemical composition of the as-obtained alloy was examined by an Axios PANalytical wavelength dispersive X-Ray fluorescence spectrometer and is given in Table 1. The obtained plate material was cut into specimens with sizes of about 20 mm × 20 mm × 5 mm. Before experiments, the samples were mechanically ground with P800–P2000 grit emery paper in 96% ethanol. After every step, the surface was ultrasonically cleaned for 5 min.

Table 1. Chemical composition of the used WE43 alloy based on X-Ray fluorescence analysis

Elemental composition [wt%]								
Al	Si	Y	Zr	Nd	Gd	Dy	Yb	Mg
0.01	0.09	4.8	0.7	2.9	0.4	0.3	0.08	Balance

As a source of PLA, Ingeo Biopolymer 3D850 from NatureWorks was used. All other chemicals used in this study were obtained from LabInvest (Belarus) or PolAura (Poland) and were of analytical reagent grade. All used solutions were prepared with deionized water with 18.2–20.0 MΩ resistivity.

2.2. Formation of coatings

The formation of CaP coatings on the surface of the WE43 alloy was performed in the solutions containing, mol/L: H_3PO_4 – 0.2; $Ca(NO_3)_2$ – 0.2; NaOH to pH 3. The temperature of the solution was kept at 70 ± 2°C. The deposition time was 60 min, after that the samples were removed from the deposition bath, rinsed under a flow of deionized water, and air-dried. In the text of this contribution, these samples are further referred to as CaP.

The PLA coatings were deposited on the surface of as-ground WE43 alloy (samples referred to as PLA) and the surface after the phosphate CaP coating was formed (samples referred to as CaP-PLA). The deposition was performed by the vertical immersion method in the solution containing 5% PLA dissolved in trichloromethane. The ejection speed was 60 mm/min. As-obtained samples were dried for 48 h at ambient temperature.

2.3. Surface analysis

The surface morphology and elemental composition of the WE43 samples before and after corrosion experiments were investigated using a JSM-5610 LV scanning electron microscope (SEM) equipped with a JED-2201energy-dispersive X-ray spectroscopy (EDX) system.

The phase analysis of the samples was performed using a D8 Advance Bruker AXS X-ray diffractometer. The obtained diffraction patterns were processed using the Match! Software and PDF-4 2022 reference base. The crystallinity index of the CaP coating was calculated based on the ratio of the total area of crystalline reflexes to the total area of all reflexes. The lattice parameters were calculated based on the Scherrer equation.

The Fourier-transform infrared spectroscopy (FTIR) spectra were acquired using a ThermoFisher Scientific Nicolet iN 10 microscope.

The X-ray photoelectron spectroscopy (XPS) measurements were performed before and after corrosion experiments using a Gammadata Scienta hemispherical analyzer SES R4000. The non-monochromatic AlKα radiation (1486.6 eV) used to excite the photoelectrons was generated

by the anode operating at 12 kV and 15 mA. The spectra analysis was performed by CasaXPS 2.3.23 software after subtraction of the Shirley-type background and fitting the experimental curve with a combination of Gaussian and Lorentzian lines of variable proportions (70:30). All obtained spectra were charge-corrected to the carbon C 1s excitation (285.0 eV).

2.4. Corrosion measurements

Corrosion experiments were performed in Hank's solution (pH 7.4) of the following composition, g/L: NaCl – 8.0; KCl – 0.2; $CaCl_2$ – 0.14; $MgSO_4 \cdot 7H_2O$ – 0.1; $MgCl_2 \cdot 6H_2O$ – 0.1; $Na_2HPO_4 \cdot 2H_2O$ – 0.06; KH_2PO_4 – 0.06; $NaHCO_3$ – 0.35; and D-glucose – 1.0 g.

Electrochemical corrosion experiments were carried out on an Autolab PGSTAT302N potentiostat/galvanostat. A traditional three-electrode setup was used. The working electrode was mounted at the bottom of the cell to avoid the accumulation of hydrogen gas, which hinders the measurement conditions. Potential values were recorded relative to a saturated Ag/AgCl reference electrode, and a Pt-mesh served as a counter electrode. The surface area of all samples was 1 cm^2. EIS measurements were carried out at the OCP over the frequency range from 10^5 to 10^{-2} Hz using a sinusoidal perturbation amplitude of 10 mV. Prior to EIS experiments, the OCP was stabilized for 30 min.

The amount of the evolved hydrogen gas was measured as described elsewhere [55]. Briefly, the non-working surface of the sample was mounted in a cold setting epoxy and then was exposed to Hank's solution in a test tube connected to one of communicating burettes. The amount of hydrogen was measured by a change in the solution volume in two communicating burettes. The monitoring of the solution pH during corrosion experiments was performed using a TitroLine easy titration system.

All corrosion measurements were performed in a thermostat at 37±0.5 °C and were at least triplicated.

3. Results and discussion

3.1. Microstructure characterization of WE43 alloy

Figure 1 shows SEM images of the surface of the as-polished WE43 alloy. The microstructure of the WE43 alloy consists of the Mg matrix with irregular-shaped intermetallic particles (IMPs). These secondary phases are either small, single constituents with sizes of ca. 10–20 μm or form agglomerates with sizes of up to 100 μm. Such microstructure is typical for the WE43 alloy [56,57]. The results of the EDX analysis showed that the alloy matrix primarily consists of magnesium with a low percentage of alloying elements (Figure 1a, area 1, Table 2). The regions around IMPs are enriched in yttrium and neodymium (Figure 1a, region 2). The EDX analysis of IMPs (Fig. 1, regions 3–10) revealed several types of Mg-rare earth intermetallics of Mg-Nd, Mg-Zr, Mg-Y, Mg-Nd-Y, Mg-Gd-Nd-Dy, and Mg-Y-Gd-Nd-Dy types with varying stoichiometry [58–61].

Surface elemental EDX maps showed that the alloy matrix is primarily composed of Mg (Fig. 2). Alloying additives of Nb, Gd, and Dy are distributed almost uniformly in the formed IMPs and their fraction is much higher than in the matrix. In the case of Y, the relative distribution over the surface was more uniform.

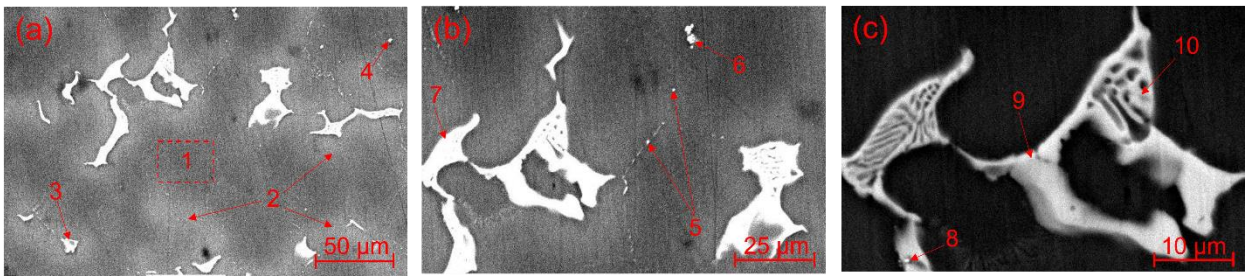

Fig. 1. SEM images of as-polished WE43 surface. Labeled regions show spots of EDX analysis reported in Table 2

Table 2. EDX analysis of the surface of as-polished WE43 Mg alloy (Analyzed areas are marked in Fig. 1)

Spot #	Elemental composition [wt%]					
	Mg	Y	Zr	Nd	Gd	Dy
WE43 surface	93.7	3.9	0.4	1.6	0.3	0.1
1	99.7	0.2	–	0.1	–	–
2	98.7	0.9	–	0.4	–	–
3	89.4	3.1	–	3.3	2.2	2.0
4	67.0	16.1	–	9.4	3.4	4.1
5	81.6	–	18.4	–	–	–
6	78.2	–	–	17.0	4.0	0.8
7	81.9	6.6	–	8.0	1.6	1.8
8	78.3	15.5	–	6.2	–	–
9	63.7	22.6	–	6.8	2.6	4.3
10	82.9	–	–	17.1	–	–

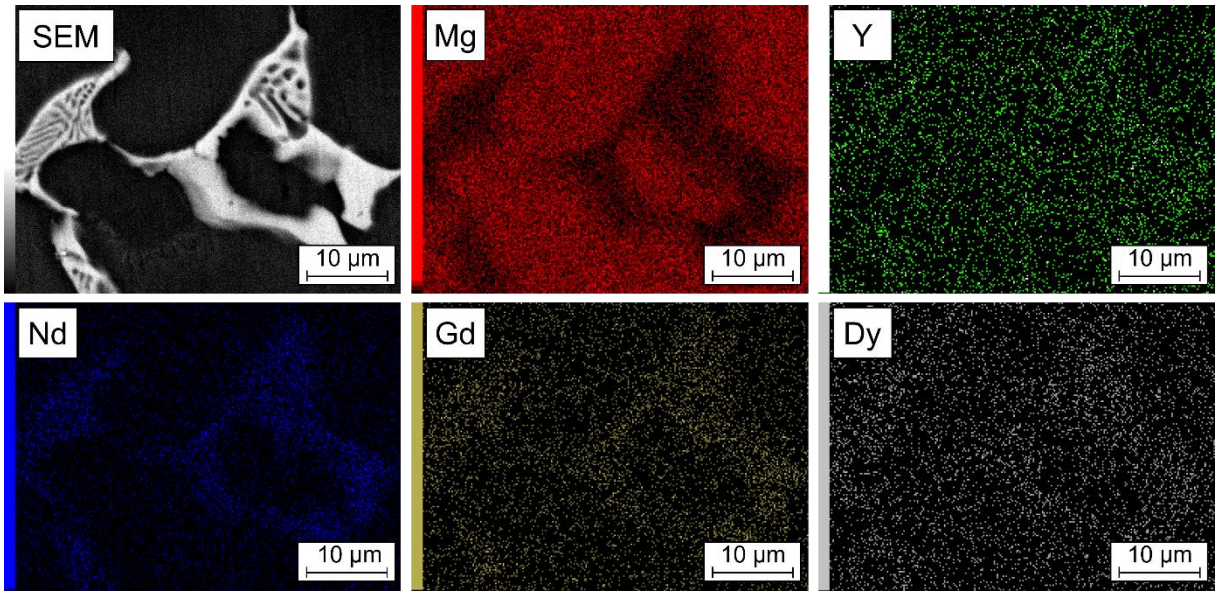

Fig. 2. Surface EDX elemental maps of as-polished WE43 alloy

3.2. Characterization of deposited coatings

3.2.1 Microstructure and morphology

The SEM images of the coated WE43 Mg alloy specimens are shown in Fig. 3. Modification of the WE43 surface in PLA solution resulted in the formation of a uniform surface layer without visible cracks or microdefects (Fig. 3a). The deposited CaP layer (Fig. 3b) is characterized by a dense fine-grained crystalline structure with a mixed morphology. The surface consists of small crystals together with a few up to ca. 50 µm-long scattered coarse crystals. The whole surface was covered with coating and no visible gaps were detected during the analysis. The CaP-PLA coating obtained in a two-stage process possessed a double-layered structure with a bottom CaP layer and a top PLA layer (Fig. 3c). The formed PLA layer fully covered the bottom CaP layer with only some visible spots where crystals of the CaP layer were protruding the top polymer coating. The EDX analysis (Table 3) showed that the formed CaP layer consists of calcium, phosphorus, and oxygen without a detectable signal from the substrate. The PLA and CaP-PLA coatings contained carbon, oxygen, and chlorine with similar elemental compositions. This may indicate that a continuous PLA coating was formed over the CaP sublayer (Fig. 3c). The presence of chlorine in the composition of these coatings is explained by the use of chloroform as a solvent of PLA.

Fig. 3. SEM images of surface morphology of (a) PLA, (b) CaP, and (c) CaP-PLA coatings

Table 3. EDX analysis of the surface of WE43 Mg alloy with obtained CaP, PLA, and CaP-PLA coatings (examined area 100 × 100 μm^2)

Sample	Elemental composition [wt%]										
	Mg	Zr	Y	Nd	Gd	Dy	Ca	P	O	C	Cl
WE43	93.7	0.4	3.9	1.6	0.3	0.1	–	–	–	–	–
CaP	–	–	1.7	–	–	–	44.4	22.2	31.7	–	–
PLA	0.3	–	–	–	–	–	–	–	41.5	56.3	2.2
CaP-PLA	–	–	–	–	–	–	–	–	41.5	55.9	2.6

Figure 4 shows SEM images and EDX elemental maps of cross-sections of the WE43 alloy coated with CaP and CaP-PLA coatings. Some defects on the substrate-coating interface can originate from the samples preparation due to polishing and reaction of the substrate with the polishing medium (96% ethanol). In the case of the CaP-PLA layers, the presence of two distinct layers was observed based on the image contrast. In both coatings, the thickness of the formed CaP layer varied in the range from 10 to 20 μm. The elemental composition of the phosphate layer is uniform throughout the coating thickness and mainly consists of Ca and P. Nevertheless, a small amount of yttrium detected in the PLA coating during the top-surface EDX analysis (Table 3) may originate from the partial dissolution of yttrium in the deposition solution and the formation of its poorly soluble oxide [60]. The thickness of the polymer layer in CaP-PLA coating is about 20 μm. The top polymer layer has good adhesion to the inner CaP layer without visible structural defects (air pockets, cracks, delamination). Note, that the thickness of both CaP and PLA coatings may slightly vary over the surface of the samples due to the heterogeneity of the surface and used deposition approaches.

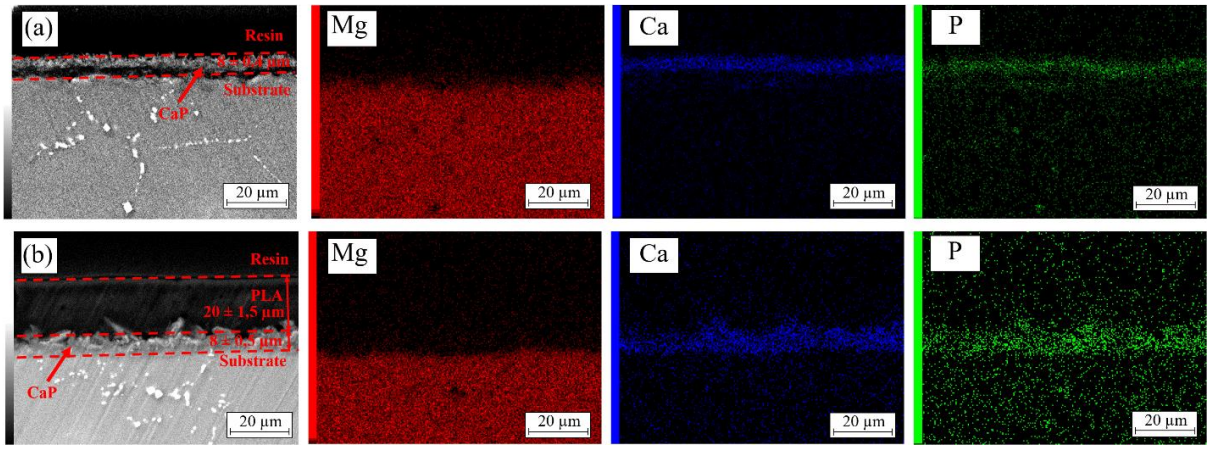

Fig. 4. SEM cross-cut images and EDX elemental maps of CaP (a) and CaP-PLA (b) coatings on WE43 Mg alloy

3.2.2 Composition and deposition mechanism

To understand the formation mechanism of CaP, PLA, and CaP-PLA coatings on the surface of the WE43 Mg alloy, their phase composition was examined. The X-ray diffraction patterns of the as-polished WE43 alloy and coated samples are shown in Fig. 5a. For the as-polished WE43 alloy, recorded reflexes correspond well to the alloy matrix (α-Mg, JCPDS card # 00-035-0821). Two reflexes of small intensity located at 2θ of 29.7 and 67.3° were assigned to $Mg_{41}Nd_5$ IMPs (JCPDS card # 00-035-0821). In the case of the PLA sample, the obtained diffractogram was identical to that of the WE43 alloy. However, a very broad low-intense peak was observed at 2θ 10–20° during the analysis of enlarged images (not shown), which might be attributed to the amorphous PLA layer [62]. After deposition of the CaP coating, additional reflexes appeared on the XRD patterns of CaP and CaP-PLA samples, which were assigned to anhydrous (monetite, JCPDS card # 00-003-0398) and dihydrated (brushite, JCPDS card # 00-011-0293) $CaHPO_4$ phases [63,64]. For the individual CaP layer, calculation of the ratio of the crystalline part of the coating to its total fraction gave crystallinity degree of 52.6%. indicates that more than half of the coating mass has an ordered crystalline structure. The obtained value confirms the structural stability of the coating. Calculated phase parameters for the main monetite phase are: crystallite size 29.93 nm, dislocation density 0.0013 $1/nm^2$. A low dislocation density

indicates a high structural stability of the coating, which can contribute to its durability and resistance to mechanical loads. Based on the change in the angle of the diffraction maximum, the microstrain parameter of the phosphate coating is $4.41 \cdot 10^{-3}$. A low microstrain value indicates the absence of significant internal stresses in the structure of the phosphate coating, which confirms its structural stability and high quality. An increase in the duration of the coating deposition at 60–100°C in aqueous solutions results in the transformation of the brushite phase into the monetite phase. No diffraction peaks corresponding to hydroxyapatite phases were indexed, which is in a good agreement with other studies [64–66]. It might be explained by the dissolution of the α-Mg matrix in the deposition bath and inhibition of hydroxyapatite growth by Mg ions [67].

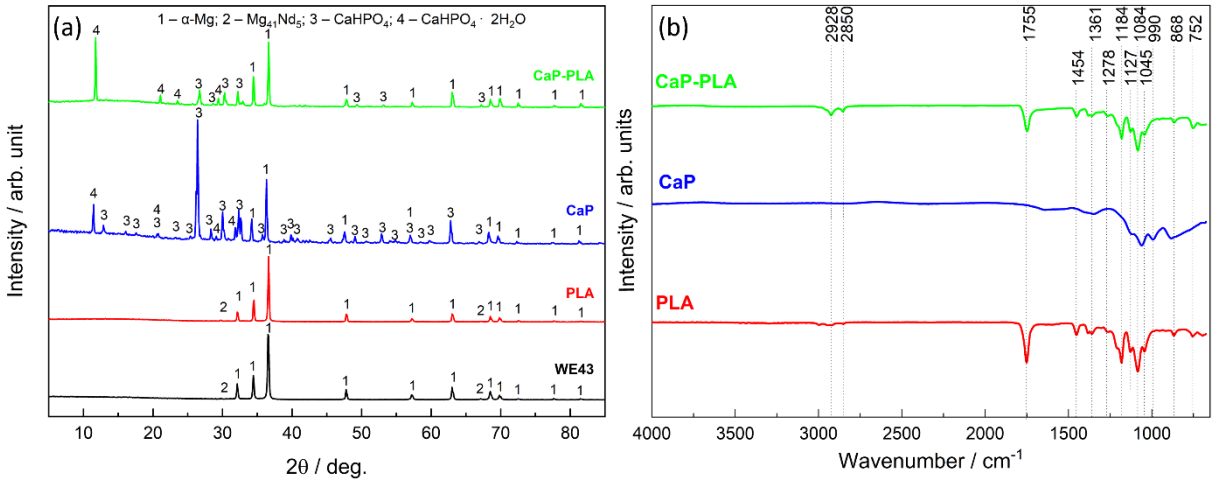

Fig. 5. (a) XRD patterns and (b) FTIR spectra of obtained PLA, CaP, and CaP-PLA coatings. Reference XRD patterns of used JCPDS cards are given in the supplementary information

The FTIR spectra of as-deposited coatings are shown in Fig. 5b. For PLA and CaP-PLA samples FTIR spectra were almost identical. The band at 752 cm^{-1} was assigned to vibrations of CH_2 group. Bands in the range of 868–990 and 1084–1140 cm^{-1} are characteristic of symmetric and asymmetric C–O–C vibrations and the band at 1045 cm^{-1} corresponds to stretching vibrations of C–O–C bonds of aliphatic esters. The band at 868 cm^{-1} indicates the formation of ordered PLA layers [68]. The band at 1184 cm^{-1} is associated with the stretching vibration of the C–O bond.

Bands in the range 1200–1250 cm^{-1} are characteristic of C–O–C bond vibrations. The band at 1755 cm^{-1} indicates the stretching vibration of the C=O carbonyl group. The band at 1454 cm^{-1} was assigned to CH_3 bending vibration. Bands at 2850 and 2928 cm^{-1} correspond to stretching vibrations in the CH_3 group [69].

The FTIR spectrum of the CaP coating exhibited vibrations in the region of 830–1160 cm^{-1}, which are typical for phosphates. A broad band in the range ca. 830–920 cm^{-1} can be assigned to symmetrical stretching of HPO_4^{2-}.[64,70] The band at 990 cm^{-1} corresponds to PO_4^{3-} antisymmetric stretching, while bands at 1063 and 1127 arise from PO_4^{3-} bending [64,71–73].

To further analyze the chemical states of the surface of all samples, XPS analysis was performed and its results are summarized in Fig. 6.

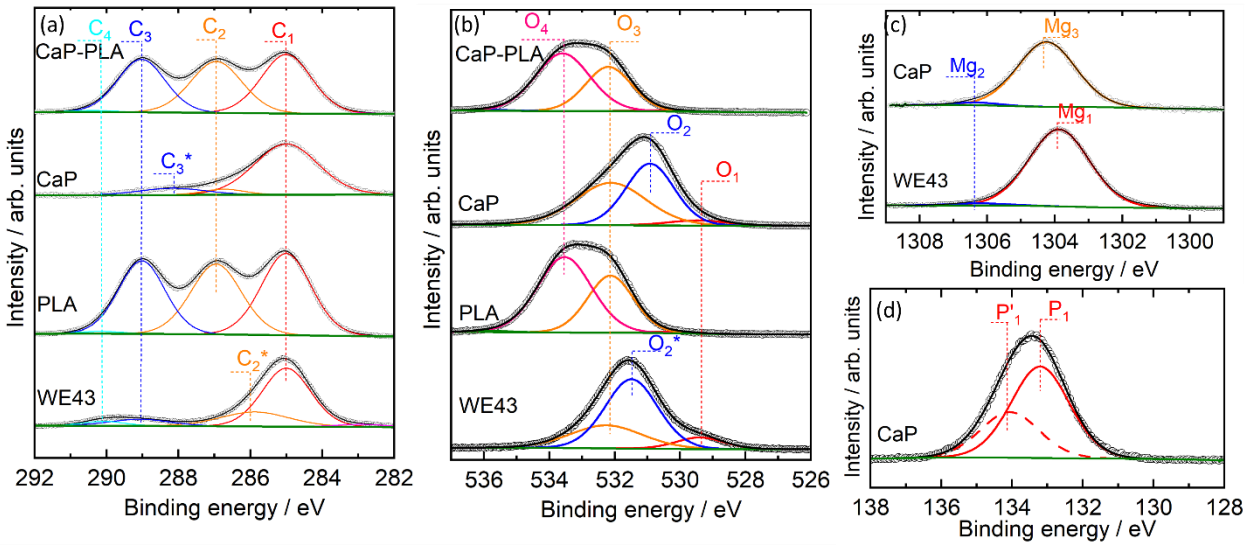

Fig. 6. High-resolution XPS spectra of as-polished WE43 alloy and obtained PLA, CaP, and CaP-PLA coatings in the binding energy range of (a) C 1s, (b) O 1s, (c) Mg 1s, and (d) P 2p

The high-resolution spectra obtained in the C 1s region (Fig. 6a) were deconvoluted into four components except for the CaP sample, where three components were extracted. The first component $C_{(1)}$ located at 285.0 eV, assigned to C–C/C–H bonds in organic compounds and contaminations [74], was found in all samples . This component is mainly associated with surface contamination [75]. The second component, $C_{(2)}$, located at 286.7 eV and $C_{(2)}$* at 285.9 eV were

assigned to C=O and C–O bonding, respectively. The next components, marked as $C_{(3)}$ and $C_{(3)}$* located at 289.0 and 288.2 eV, respectively, were assigned to O–C=O groups. In the case of the PLA and CaP-PLA samples, this component corresponds to the PLA layer [76]. For the CaP sample, it is assigned to -COO-Ca [77] and most probably originated from surface contamination. The last component, $C_{(4)}$, located at 290.1 eV, originated from the surface contamination of carbonates.

The high-resolution O 1s spectra (Fig. 6b) were deconvoluted into several components. Components $O_{(1)}$, $O_{(2)}$, and $O_{(2)}$*, located at 529.4, 530.9, and 531.5 eV, respectively, were assigned to oxides, mostly MgO (components $O_{(2)}$, and $O_{(2)}$*). The component $O_{(3)}$ at 532.3 eV corresponds to OH-groups in $Mg(OH)_2$ [75]. The last component $O_{(4)}$ at 533.5 eV was observed on the surface of the PLA and CaP-PLA samples and corresponds to the C–O bonds in the PLA layer [78].

The signal in the binding energy range of Mg 1s was detected only for WE43 and CaP samples (Fig. 6c). The main $Mg_{(1)}$ component at 1304.1 eV for the WE43 sample was assigned to $Mg(OH)_2$. A smaller component $Mg_{(2)}$ (1306.3 eV) was assigned to magnesium carbonate [79]. For the CaP sample, the main component $Mg_{(3)}$ (1304.3 eV) was identified as a signal from magnesium phosphates/$Mg(OH)_2$.

The P 2p spectrum for the CaP sample was deconvoluted into one doublet with P $2p_{3/2}$ and P $2p_{1/2}$ binding energies of 133.2 and 134.1 eV (marked as P and P', respectively), assigned to phosphates (Fig. 6d). In the case of the CaP-PLA sample, the surface was fully covered by the PLA layer and no signal of P was detected.

The results of FTIR and XPS experiments suggest higher amount of CH_3 groups of PLA on the surface of CaP-PLA samples (increased intensity of FTIR bands at 2850 and 2928 cm^{-1} in Fig. 5b) and lower amount of C=O groups (decreased intensity of FTIR band at 1755 cm^{-1} in Fig. 5b) comparing to a single PLA layer. It is also supported by the XPS spectra of O (Fig. 6b) and C (Fig. 6c), where a lower amount of C_3 (O–C=O) and O_4 (C–O) components were registered for

CaP-PLA coatings. This suggests different mechanisms of the adhesion of PLA to the blank WE43 substrate and CaP-coated substrate during the deposition process.

The obtained experimental data were supplemented by theoretical calculations. Fig. 7 represents the equilibrium concentration diagram of ionic species and the volume fraction diagram of phosphate ions in the solution for the deposition of CaP coating. Calculations were performed without applying external potential, simulating fractions of the components corresponding to the aqueous conditions. However, it was assumed that Mg^{2+} ions are present in the solution due to the oxidation of the WE43 alloy. The concentration diagram (Fig. 7a) shows that several types of calcium and magnesium phosphates can be formed in the solution, while at very low pH aqueous Ca^{2+} and Mg^{2+} ions predominate. A more detailed fraction diagram for phosphate ions (Fig. 7b) revealed that soluble monocalcium phosphate $CaH_2PO_4^+$ ions will predominate in the pH range up to ca. 3.2. From pH ca. 2.9 the fraction of insoluble hydrated calcium phosphate $CaHPO_4 \cdot 2H_2O$ starts to increase and it is the most expected compound in the range of pH up to ca 6.2. At near-neutral conditions, mainly $Ca_5(PO_4)_3OH$ compound is expected. As Mg^{2+} ions were also considered in calculations, a minor fraction of $MgH_2PO_4^+$ ions in the pH range up to 6.5 and $MgHPO_4 \cdot 3H_2O$ starting from pH ca. 5.6 can be expected.

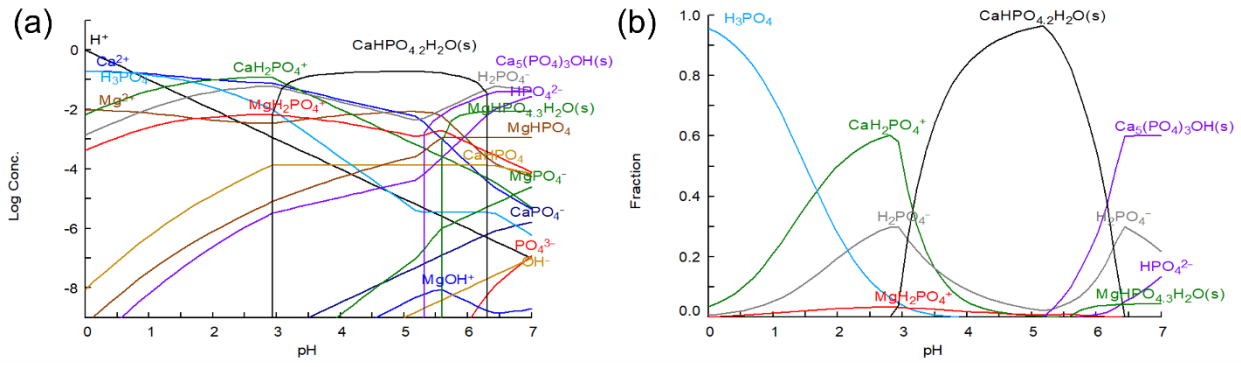

Fig. 7. (a) Concentration diagram and (b) volume fraction diagram of phosphate ions for an aqueous solution containing 0.2 M PO_4^{3-}, 0.2 M Ca^{2+}, and 0.01 M Mg^{2+} ions as a function of pH. No external potential was applied in calculations. The data were calculated using the Medusa software [80]

Based on the experimental results and theoretical calculations, a formation mechanism of the CaP layer on the surface of the WE43 alloy can be described as follows. Upon immersion of the WE43 alloy in the deposition bath (pH 3), the surface of the Mg alloy dissolves rapidly according to the scheme:

$$Mg \rightarrow Mg^{2+} + 2e^{-} \quad (1)$$

$$2H^{+} + 2e^{-} \rightarrow H_2 \quad (2)$$

The process generates excessive amounts of gaseous hydrogen. Consumption of H^+ on Eq. (2) results in local alkalization of the Mg alloy/electrolyte interface and an increase in pH. According to the thermodynamic data (Fig. 7), this would trigger the reaction of metal ions with $H_2PO_4^-$ and the formation of insoluble $CaHPO_4 \cdot 2H_2O$ on the surface:

$$Ca^{2+} + H_2PO_4^{-} + 2H_2O \rightarrow CaHPO_4 \cdot 2H_2O + H^{+} \quad (3)$$

Our experimental data also indicated that anhydrous $CaHPO_4$ can be formed on the surface according to the equation:

$$Ca^{2+} + H_2PO_4^{-} \rightarrow CaHPO_4 + H^{+} \quad (4)$$

Taking into account solubility product constants, K_{sp}, of $CaHPO_4$ (2.7×10^{-7}), $CaHPO_4 \cdot 2H_2O$ (2.6×10^{-7}) [81], and $MgHPO_4$ (1.2×10^{-3}) [65] it is expected that only calcium phosphates will be included in the formed coating.

The remnant $H_2PO_4^-$ ions can also react with OH^- to form HPO_4^{2-} and then PO_4^{3-} ions, which can form insoluble salts $Ca_3(PO_4)_2$ and $Mg_3(PO_4)_2$ [82]:

$$3Ca^{2+} + 2PO_4^{3-} \rightarrow Ca_3(PO_4)_2 \quad (5)$$

$$3Mg^{2+} + 2PO_4^{3-} \rightarrow Mg_3(PO_4)_2 \quad (6)$$

3.3 Corrosion in Hank's solution

The corrosion properties of the WE43 alloy with and without surface modification were evaluated in Hank's solution.

The results of the EIS measurements in the form of Nyquist plots are shown in Fig. 8. The impedance response of the bare WE43 alloy in Hank's solution (Fig. 8a) is typical for this type of Mg alloys [57]. The Nyquist plot characteristically displayed one small capacitive loop at high

frequencies, a large depressed capacitive loop at medium to low frequencies, and an inductive tail at low frequencies. The capacitive response is associated with the charge transfer processes, while the inductive response is typically associated with relaxation processes of adsorbed charged corrosion intermediates [83]. In the case of coated samples (Fig. 8b), impedance spectra showed two capacitive semicircles without inductive region, which indicates better corrosion resistance of the surface. The best corrosion resistance was provided by CaP-PLA coating. To quantitatively analyze the EIS data, equivalent circuits shown in Fig. 8c were used. In these circuits, the constant phase element CPE, with two parameters, the CPE constant Y and the exponent n obtained from the data fitting, was used. Other circuit's elements include R_s as the solution resistance, CPE_1 as the capacitive response of the surface film (coating or corrosion products), R_2 as the surface film resistance, CPE_2 as the double-layer capacitive response, and R_3 as the charge transfer resistance [57,83]. Circuit *1* used for the bare WE43 alloy additionally contains L_1 and R_1 elements, which are the inductance and resistance parameters involving adsorbed intermediates that give rise to the impedance response at low frequencies. The quantitative assessment of the surface resistance was performed based on the values of the polarization resistance, R_p, calculated as shown in Fig. 8c. The obtained fit parameters and calculated R_p values are summarized in Table 4.

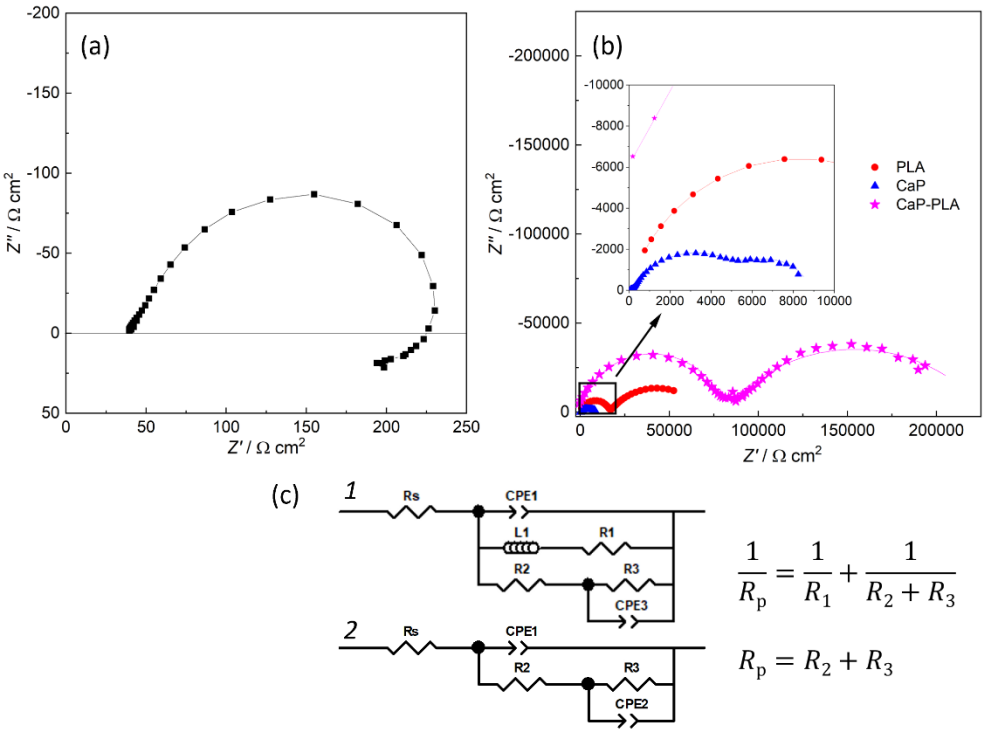

Fig. 8. Nyquist EIS plots in Hank's solution of WE43 alloy (a) and obtained PLA, CaP, and CaP-PLA coatings (b). Symbols represent experimental data and lines are results of spectra fitting using equivalent circuits shown in (c)

From the fitting results (Table 4), the highest value of R_p was observed for a two-layer CaP-PLA coating. The high protective ability of the CaP-PLA coating most probably originates from two factors: i) different adhesion of the PLA layer to the CaP layer as compared to the untreated WE43 alloy (Table S1 and Fig. S1 in the Supplementary Information), and ii) filling of CaP microcracks with the polymer layer, which further prevents direct contact of the corrosive medium with the magnesium substrate. However, it should be noted that the these values were extracted from two different circuits so caution should be taken in the direct comparison of the quantitative data [84]. Moreover, electrochemical methods can overestimate the corrosion resistance of Mg alloys [55,83,85]. Therefore, hydrogen evolution and pH of Hank's solution were monitored for 14 days.

Table 4. Fitting data extracted from EIS data

Sample	L / H cm^2	R_1 / Ω cm^2	Y_1 / Ω^{-1} cm^{-2} s^n	n_1	R_2 / Ω cm^2	Y_2 / Ω^{-1} cm^{-2} s^n	n_2	R_3 / Ω cm^2	R_p / Ω cm^2
WE43	41.9 ± 5.7	534.4 ± 28.1	(7.2 ± 2.7)·10^{-5}	0.81 ± 0.11	224. 2 ± 34.8	(1.8 ± 0.3)·10^{-3}	0.80 ± 0.15	12.9 ± 4.7	164.2
CaP	–	–	(1.4 ± 0.3)·10^{-5}	0.70 ± 0.09	5793.4 ± 148.2	(3.9 ± 1.8)·10^{-4}	0.82 ± 0.07	2894.4 ± 58.1	8687.8
PLA	–	–	(6.4 ± 1.6)·10^{-9}	0.84 ± 0.12	16543.7 ± 2534.9	(1.4 ± 0.6)·10^{-5}	0.60 ± 0.05	52866.0 ± 12573.7	69409.7
CaP-PLA	–	–	(1.8 ± 0.4)·10^{-9}	0.88 ± 0.05	79859.1 ± 5024.0	(6.6 ± 2.3)·10^{-6}	0.67 ± 0.18	148510.2 ± 22455.0	228369.3

The results of the hydrogen evolution test are shown in Fig. 9. The volume of hydrogen evolved in Hank's solution containing bare WE43 alloy gradually increased with time. After 5 days, the hydrogen release rate decreased slightly, which may be a sign of the partial surface passivation by corrosion products. In the case of treated samples, the volume of the evolved hydrogen significantly decreased. In the case of CaP and CaP-PLA coatings almost no hydrogen was evolved during 14 days of the experiment. This indicates the high protective ability of the formed coatings.

In near-neutral Hank's solution (initial pH 7.4 ± 0.2), corrosion of the WE43 Mg alloy consists of the anodic dissolution of Mg matrix (Eq. (1)) and the cathodic reaction of hydrogen evolution (Eq. (7)):

$$2H_2O + 2e^- \rightarrow H_2 + 2OH^- \quad (7)$$

with the overall reaction (Eq. (8))

$$Mg + 2H_2O + 2e^- \rightarrow Mg^{2+} + H_2 + 2OH^- \quad (8)$$

Therefore, the evolution of hydrogen is possible when the substrate is in contact with Hank's solution. In the case of a single PLA layer its degradation results in fast contact of the Mg substrate with the solution. Oppositely, in the case of the CaP-PLA layer, hydrogen evolution will be initiated only after degradation of both PLA and CaP layers. That is the main reason for the improved corrosion resistance.

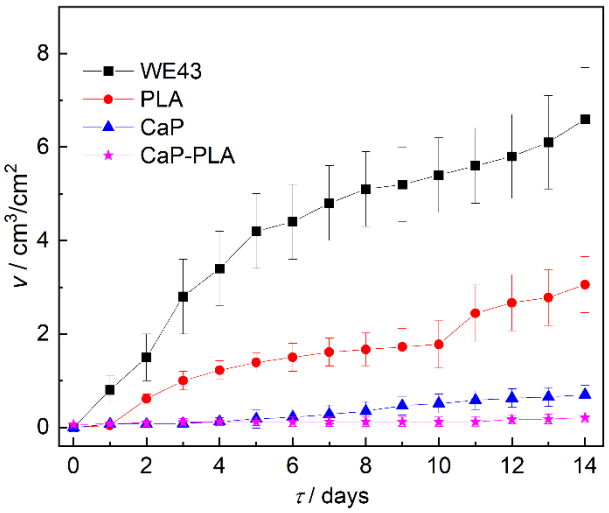

Fig. 9. Hydrogen evolution as a function of the immersion time of WE43 alloy and obtained PLA, CaP, and CaP-PLA coatings in Hank's solution

Figure 10 shows the dependence of the change in the pH of Hank's solution on the exposure time of the investigated WE43 alloy specimens. The microstructure of the WE43 alloy consists of the Mg matrix with irregular-shaped IMPs (Figs. 1, 2), and these IMPs are cathodic relative to the Mg matrix [57]. Owing to a large difference in the Volta-potentials [57], galvanic corrosion caused by the second phases usually dominates in the corrosion rate of Mg alloys [86,87]. Magnesium ions Mg^{2+} formed by Eq. (1) can interact with hydroxide-ions formed by Eq. (7) to produce poorly soluble magnesium hydroxide $Mg(OH)_2$. Therefore, the change in the pH of the corrosive medium

associated with the occurrence of the cathodic process on Eq. (8) can be used as a measure of the corrosion rate of magnesium alloys. In the case of the untreated WE43 alloy, the pH of the electrolyte gradually increased reaching the value of 10.4 after 14 days of exposure. The PLA sample showed a very similar trend of the change in the pH with time, indicating poor long-term corrosion resistance of the single PLA layer, despite the rather high protective ability obtained in the EIS experiments (Fig. 8, Table 4). In turn, the pH of Hank's solution where CaP and CaP-PLA coatings were exposed did not increase so prominently. According to the literature [87,88], phosphate conversion coatings preferentially precipitate on the cathodic sites of the surface, effectively suppressing the cathodic reaction. The pH of the Hank's solution increased for the first three days of the experiment and then almost did not change, reaching the value of 8.7 and 7.9 after 14 days of exposure of the CaP and CaP-PLA samples in Hank's solution, respectively. This indicates a high corrosion resistance of CaP and especially combined CaP-PLA coatings.

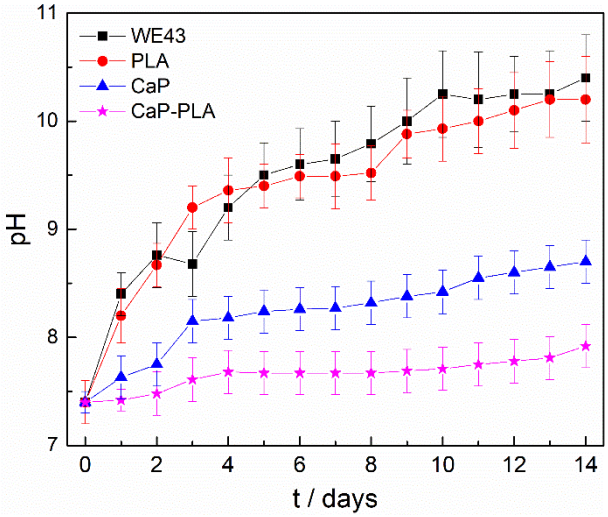

Fig. 10. Evolution of pH of Hank's solution during 14 days of exposure of WE43 Mg alloy with different surface treatment

3.4 Post-corrosion surface analysis

For a more detailed examination of the protective properties, a post-corrosion analysis of the surface of the obtained coatings was carried out after 14 days of exposure to Hank's solution.

The results of the XRD analysis of all examined samples after 14 days of exposure to Hank's solution are presented in Fig. 11a. The most significant changes were observed for the

WE43 and PLA samples. In both cases, new strong reflexes corresponding to $Mg(OH)_2$ (JCPDS card # 00-044-1482) were observed on the XRD patterns. Diffractograms of the CaP and CaP-PLA samples were similar to those shown in Fig. 5a for as-obtained samples.

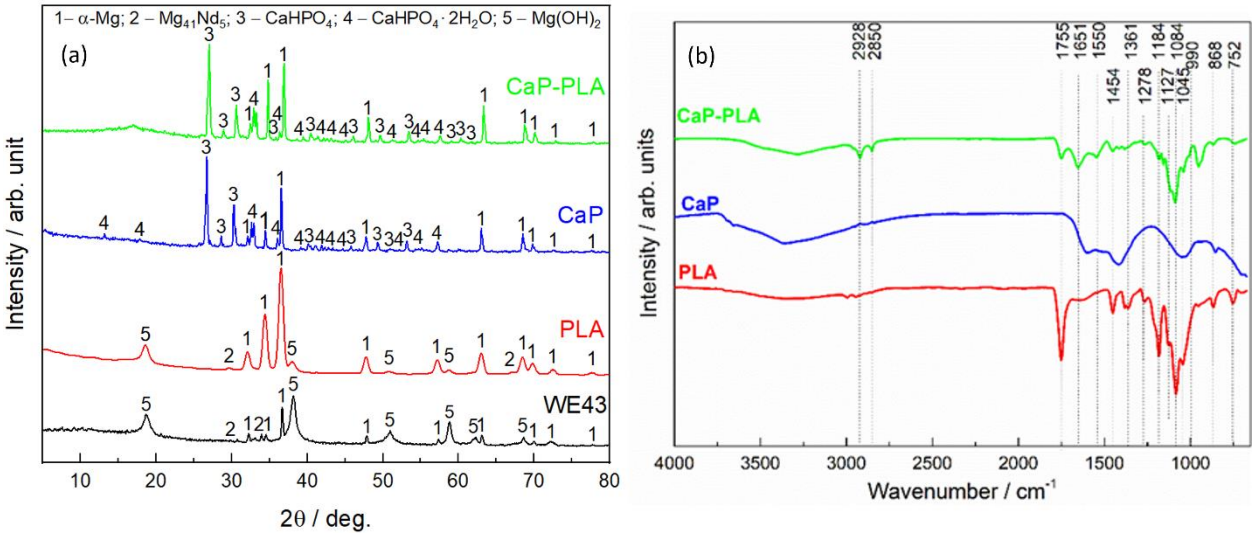

Fig. 11. (a) XRD patterns and (b) FTIR spectra of PLA, CaP, and CaP-PLA coatings after 14 days of exposure to Hank's solution. Reference XRD patterns of used JCPDS cards are given in the supplementary information

The FTIR spectra of the coatings after 14 days of corrosion in Hank's solution are shown in Fig. 11b. The general appearance of the spectra remained similar for all specimens. For the PLA and CaP-PLA coatings, an increase in the intensity of the bands at 1278 and 1184 cm^{-1} associated with asymmetric C–O–C stretching vibrations and asymmetric CH_3 vibrations is observed. Such changes can be explained by an increase in the crystallinity of the PLA coating [89,90]. The appearance of the band at 1550 cm^{-1} corresponds to O_2 vibrations. In the case of the CaP coating, an additional wide band at 1620–1600 cm^{-1} is observed, which is due to the presence of OH-groups of water. Spectra of all samples also show wide bands in the region 3670–3020 cm^{-1}, which correspond to the stretching vibrations of OH- groups of water.

To further evaluate changes in the surface chemistry after long-term corrosion analysis, XPS spectra were recorded. Due to the high amount of water adsorbed by the PLA sample, it was

not possible to reach the level of vacuum in the equipment chamber required for the XPS measurement. Therefore, Fig. 12 shows the results for WE43, CaP, and CaP-PLA samples only.

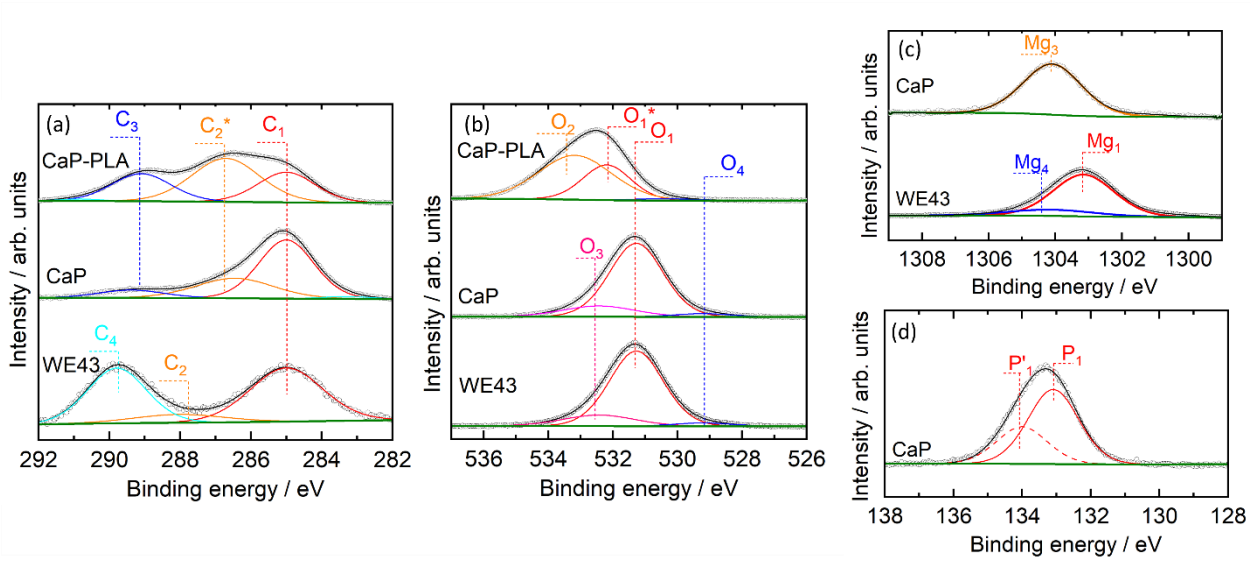

Fig. 12. High-resolution XPS spectra in the binding energy range of (a) C 1s, (b) O 1s, (c) Mg 1s, and (d) P 2p of WE43 alloy, CaP, and CaP-PLA coatings after corrosion experiments in Hank's solutions

The general appearance of C 1s spectra (Fig. 12a) and components assignment remained the same as for the as-obtained samples (Fig. 6a). For the WE43 sample, the relative fraction of the $C_{(4)}$ component increased significantly, indicating higher surface amounts of magnesium carbonate and intensive corrosion of the alloy in Hank's solution. For CaP and CaP-PLA samples, the most notable increase in the surface fraction corresponded to the $C_{(2)}$* component, assigned to C–O bonding. In the high-resolution O 1s spectra (Fig. 12b), $O_{(1)}$ became the main component for WE43 and CaP samples. For the CaP-PLA sample, $O_{(1)}$ and $O_{(2)}$ remained the main components. The XPS spectra of the WE43 and CaP samples contained additional component $O_{(3)}$ at 532.6 eV, which was assigned to OH- groups or absorbed water. The Mg 1s spectrum for the WE43 sample possessed a new component $Mg_{(4)}$ located at 1304.3 eV and associated with $Mg(OH)_2$ (Fig. 12c) [55]. The P 2p spectrum (Fig. 12d) was similar to that before corrosion experiments. Summarizing, the surface chemistry of the WE43 alloy changed significantly due to the corrosion attack, while

the surface of modified samples remained almost the same, indicating their high corrosion resistance.

The post-corrosion morphologies of the untreated WE43 alloy and coated samples are shown in Fig. 13. A thick layer of corrosion products was formed on the surface of the WE43 sample (Fig. 13a). This surface layer is non-uniform and contains a network of microcracks, due to the release of hydrogen and the internal stresses. The layer itself could not provide reliable corrosion protection of the substrate. The formation of wedge-shaped cracks can be explained by stress concentration at the top layer of dislocations near the grain boundary of the alloy. The surface of the CaP sample after 14 days of exposure to the Hank's solution (Fig. 13b) did not undergo significant morphological changes. The surface of the samples coated with PLA (Fig. 13c) had two characteristic surface regions. The first one, clearly visible at smaller magnifications represents the surface regions covered with corrosion products. The second one appears as a network of micropores, which indicates polymer degradation in Hank's solution. Such a morphology supports the results of the pH monitoring (Fig. 10), confirming the low corrosion resistance of the PLA film. In the case of the CaP-PLA sample (Fig. 13d), the morphology of the top surface layer was similar to the PLA sample and revealed degradation of the polymer layer. The formed pores were larger in diameter and the bottom CaP layer was visible in some spots. However, the surface was clear from corrosion products, since the bottom CaP layer remained intact.

The point EDX analysis (Table 5) of the selected surface regions (marked in Fig. 13) showed that the layer of corrosion products formed on the surface of the untreated WE43 Mg alloy (Table 5, spot 1) is rich in Mg and O, supporting deposition of an oxide-hydroxide layer of corrosion products on the surface. The presence of P and Ca indicates that this layer also contains poorly soluble calcium and magnesium phosphates, originating from the composition of the Hank's solution. The composition of the CaP surface (Table 5, point *2*) practically did not change during corrosion testing and is comparable to the initial sample (Table 3). The elemental

556 composition of PLA and CaP-PLA samples is presented by mostly C and O, with minor amounts
557 of P and Cl. In the case of the PLA sample, spots identified as corrosion products contained high
558 amounts of Na and Cl, suggesting severe corrosion attack in these regions.

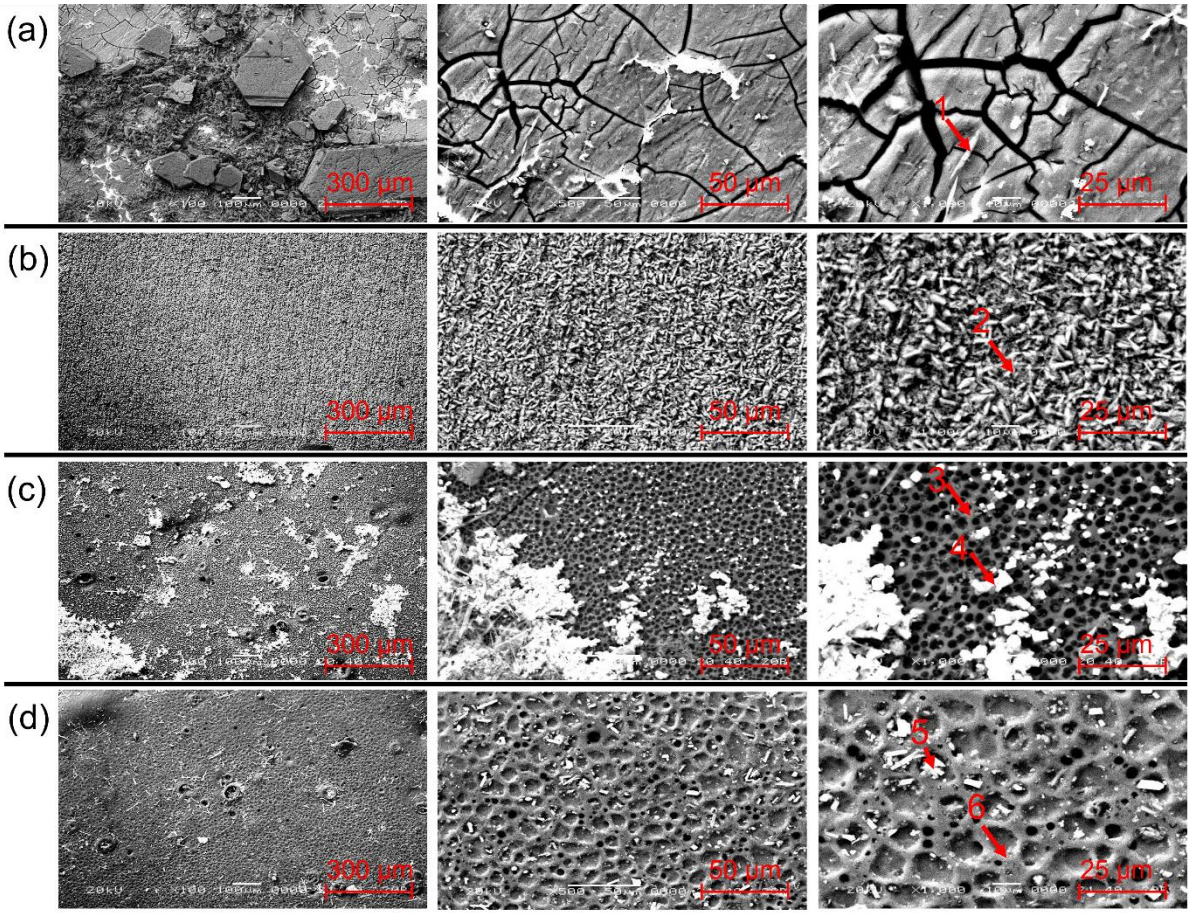

559

560 **Fig. 13.** SEM images of surface morphology of (a) untreated WE43, (b) CaP, (c) PLA, and (d)
561 CaP-PLA coatings after 14 days of exposure to Hank's solution. Arrows indicate regions of point
562 EDX analysis listed in Table 5

563

564 **Table 5**. Point EDX analysis of the surface of WE43 Mg alloy without and with obtained CaP,
565 PLA, and CaP-PLA coatings after 14 days of exposure to Hank's solution (examined points are
566 marked in Fig. 13)

Point of analysis	Elemental composition [wt%]										
	Mg	Y	Nd	Gd	Dy	Ca	P	O	C	Cl	Na
1	32.9	1.3	5.0	1.4	0.9	1.4	12.8	38.3	–	–	–
2	17.4	0.6	0.1	–	–	16.7	11.9	48.2	–	–	5.1
3	0.9	–	–	–	–	–	0.2	41.8	55.6	1.6	
4	0.5	–	–	–	–	–	0.2	15.7	48.7	6.5	28.4
5	0.3	–	–	–	–	2.1	1.5	42.9	52.4	0.9	–

6	–	–	–	–	–	0.1	0.2	42.0	55.7	1.1	–

Figure 14 shows SEM cross-cut images of the examined samples after 14 days of corrosion testing in Hank's solution. The layer of corrosion products formed on the surface of the untreated WE43 Mg alloy (Fig. 14a) has a thickness of about 15 µm. The cracks observed in the top-surface SEM observations (Fig. 13a) reach the metal substrate. Interestingly, the results of the point EDX analysis confirmed that the layer of corrosion products also contains inclusions reach in Y, Gd, Dy, and Nd (Fig. 14a, point *1*, Table 6), which are alloying elements in the WE43 alloy and form IMPs in its microstructure. In the case of the CaP coating (Fig. 14b) the layer morphology did not reveal significant changes. However, cross-cut observations revealed the presence of a local corrosion attack similar to filiform corrosion. The best results were obtained for the CaP-PLA sample, which does not undergo visible structural changes after 14 days of corrosion (Fig. 14d).

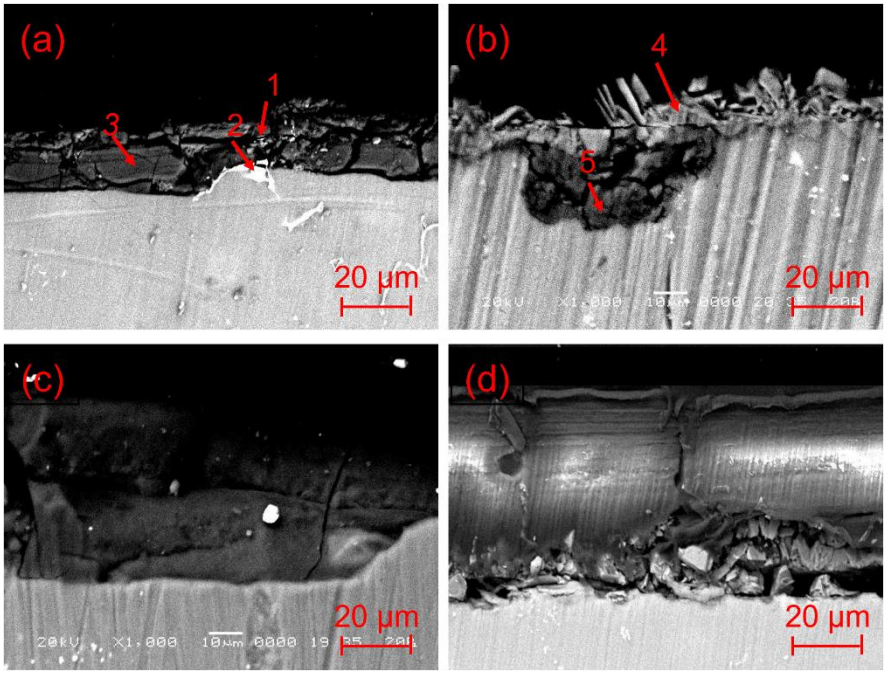

Fig. 14. SEM cross-cut images of (a) untreated WE43, (b) CaP, (c) PLA, and (d) CaP-PLA coatings after 14 days of exposure to Hank's solution

Mechanisms of corrosion degradation of the obtained coatings are schematically illustrated in Fig. 15. The results of the corrosion experiments confirmed that the most severe corrosion attack was observed for the untreated WE43 alloy. In this case, the Mg matrix of the alloy is dissolved,

584 while the most severe corrosion attack is initiated and proceeds along the Mg matrix/IMPs
585 interface due to galvanic coupling [57,91]. The mechanism of the destruction of cathodic IMPs
586 containing rare-earth elements is not so straightforward and the most expected mechanism is the
587 one similar to the iron re-deposition explained in several previous studies [92–94]. Briefly,
588 cathodic IMPs are first detached from the metallic substrate by undermining or hydrogen bubbles
589 due to the process described by Eq. (7). Later on, rare-earth-rich particles are dissolved in the
590 electrolyte forming soluble compounds, which are then reduced to metallic rare-earth or react with
591 the solution compounds (for example, phosphates) to form insoluble precipitates.
592
593 **Table 6.** Point EDX analysis of the crosscut areas of WE43 Mg alloy without and with CaP
594 coatings after 14 days of exposure to Hank's solution (examined points are marked in Fig. 14)

Point of analysis	Elemental composition [wt%]							
	Mg	Y	Nd	Gd	Dy	Ca	P	O
1	77.4	8.7	7.8	2.2	3.9	1.4	7.9	–
2	76.8	15.4	3.9	1.5	2.4	–	–	–
3	44.2	–	–	–	–	0.3	9.9	–
4	40.0	–	–	–	–	38.2	21.8	–
5	43.3	2.3	1.3	–	–	0.2	1.2	51.8

595
596 The corrosion mechanism was different in the case when CaP and/or PLA coatings were
597 deposited on the surface. In these cases, the WE43 alloy surface was protected by the formed
598 coatings. However, individual coatings possess local corrosion spots. In the case of the CaP layer,
599 these spots were up to 20 μm deep and hidden under the CaP layer. The occurrence of such
600 corrosion spots can be explained by the presence of microcracks in the CaP structure, where
601 contact of the metal matrix with the electrolyte is possible.
602 The low protective ability of the PLA coating can be explained by its high water
603 permeability. Consequently, during long-term corrosion, a corrosive medium can reach the
604 metallic substrate, which leads to the initiation of corrosion under the polymer film. At the same
605 time, the obtained PLA layer retained its integrity, and no delamination was observed.

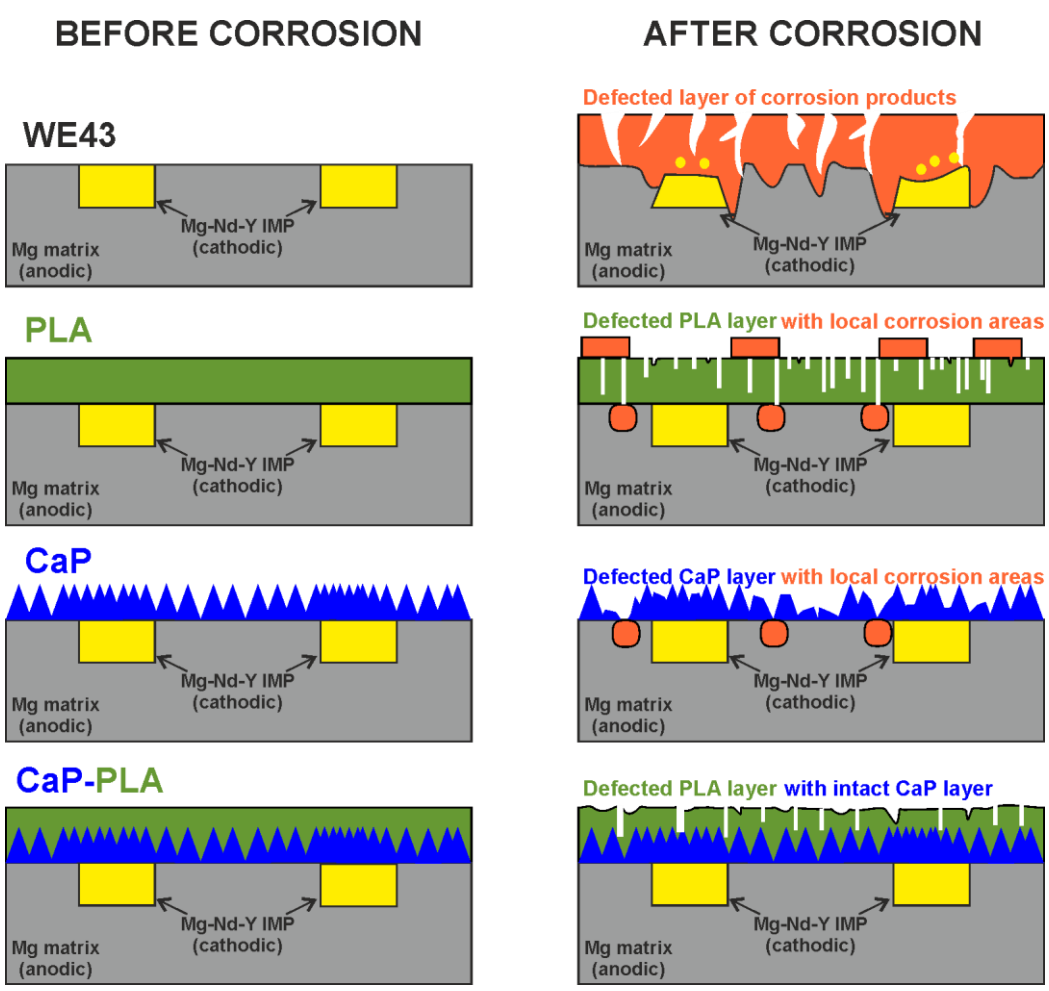

Fig. 15. Schematic representation of the formed layers before (to the left) and after (to the right) exposure to Hank's solution for 14 days

The best results were observed for the dual CaP-PLA coating. The improvement in the corrosion resistance is achieved by filling pores and cracks in the CaP layer with the top PLA coating, which is clearly seen on SEM images before (Fig. 3c) and after (Fig. 13d) corrosion tests.

4. Conclusions

In this work, the effect of surface pretreatment by a calcium phosphate and/or PLA layer on the corrosion properties of the WE43 magnesium alloy was examined. The high corrosion protection effectiveness of all coatings was observed and correlated with the surface film structure. The following conclusions can be drawn:

1. SEM and EDX analysis revealed that the WE43 alloy has a complex microstructure, which contains an Mg matrix and Mg-rare earth IMPs (Nd, Gd, Dy, Y, Zr).

2. A dense and fine-grained conversion CaP coating mainly consisting of $CaHPO_4 \cdot 2H_2O$ and $CaHPO_4$ with a thickness of 10–20 μm was formed on the surface of the WE43 alloy. The corrosion rate of the as-treated WE43 alloy in Hank's solution decreased by a factor of 10. In the long-term corrosion experiments, the CaP layer did not undergo significant structural, morphological, and phase changes. However, due to local coating defects (cracks, pores), several local corrosion spots were observed, which is in good accordance with an increase in the pH of Hank's solution by ≈1.1.

3. Deposition of the PLA layer on the surface of the WE43 alloy results in the formation of a uniform polymer coating with a thickness of about 20 μm. The corrosion rate of the as-treated WE43 alloy in Hank's solution decreased by a factor of 100. However, due to high water permeability and low adhesion to the substrate, PLA coating does not provide reliable corrosion protection of the WE43 substrate in long-term corrosion experiments.

4. A two-layer CaP-PLA coating provided reliable corrosion protection with corrosion current density decreasing by a factor of 500 compared to the untreated WE43 alloy, and by a factor of 53 compared to the CaP sample, which is explained by the filling of the local surface defects in the bottom phosphate layer by the top polymer layer. After long-term corrosion tests in Hank's solution, the two-layer coating did not show visible structural changes, and the pH of the solution practically did not change in time, which indicates the high protective properties of the CaP-PLA coating.

Declarations of interest

The authors declare that they have no known competing financial interests or personal relationships that could have appeared to influence the work reported in this paper.

Data availability

The raw/processed data required to reproduce the findings of this study are available from the corresponding authors upon reasonable request.

Acknowledgments

Dzmitry Kharytonau gratefully acknowledges the partial financial support of this study by the National Science Centre (Poland) under research Grant Sonatina no. 2021/40/C/ST5/00266.

CRediT authorship contribution statement

Andrei V. Paspelau: Conceptualization, Methodology, Investigation, Formal analysis, Visualization, Validation, Writing – Original Draft;

Aliaksandr A. Kasach: Conceptualization, Methodology, Investigation, Formal analysis, Visualization, Validation, Writing – Original Draft;

Jacek Gurgul: Investigation;

Grzegorz Mordarski: Investigation;

Konrad Skowron: Investigation;

Irina I. Kurilo: Methodology, Formal analysis, Writing – Review & Editing;

Dzmitry S. Kharytonau: Project administration, Funding acquisition**,** Conceptualization, Methodology, Investigation, Data Curation, Formal analysis, Visualization, Validation, Funding acquisition, Supervision; Writing – Original Draft; Writing – Review & Editing.

References

[1] V. Brailovski, P. Terriault, Metallic Porous Materials for Orthopedic Implants: Functional Requirements, Manufacture, Characterization, and Modeling, in: Ref. Modul. Mater. Sci. Mater. Eng., Elsevier, 2016. https://doi.org/10.1016/B978-0-12-803581-8.03892-3.

[2] N.S. Manam, W.S.W. Harun, D.N.A. Shri, S.A.C. Ghani, T. Kurniawan, M.H. Ismail, M.H.I. Ibrahim, Study of corrosion in biocompatible metals for implants: A review, J. Alloys Compd. 701 (2017) 698–715. https://doi.org/10.1016/j.jallcom.2017.01.196.

[3] K. Katti, D. Verma, D. Katti, Materials for joint replacement, in: Jt. Replace. Technol.,

675 Elsevier, 2008: pp. 81–104. https://doi.org/10.1533/9781845694807.1.81.
676 [4] M.P. Staiger, A.M. Pietak, J. Huadmai, G. Dias, Magnesium and its alloys as orthopedic
677 biomaterials: A review, Biomaterials. 27 (2006) 1728–1734.
678 https://doi.org/10.1016/j.biomaterials.2005.10.003.
679 [5] Metals for medical implants, in: Mech. Biomater., Cambridge University Press, 2011: pp.
680 26–69. https://doi.org/10.1017/CBO9780511977923.005.
681 [6] L. Zhang, G. Yang, B.N. Johnson, X. Jia, Three-dimensional (3D) printed scaffold and
682 material selection for bone repair, Acta Biomater. 84 (2019) 16–33.
683 https://doi.org/10.1016/j.actbio.2018.11.039.
684 [7] S. Bose, D. Ke, H. Sahasrabudhe, A. Bandyopadhyay, Additive manufacturing of
685 biomaterials, Prog. Mater. Sci. 93 (2018) 45–111.
686 https://doi.org/10.1016/j.pmatsci.2017.08.003.
687 [8] M. Geetha, A.K. Singh, R. Asokamani, A.K. Gogia, Ti based biomaterials, the ultimate
688 choice for orthopaedic implants – A review, Prog. Mater. Sci. 54 (2009) 397–425.
689 https://doi.org/10.1016/j.pmatsci.2008.06.004.
690 [9] D. Campoccia, L. Montanaro, C.R. Arciola, The significance of infection related to
691 orthopedic devices and issues of antibiotic resistance, Biomaterials. 27 (2006) 2331–2339.
692 https://doi.org/10.1016/j.biomaterials.2005.11.044.
693 [10] L.-Y. Cui, X.-H. Fang, W. Cao, R.-C. Zeng, S.-Q. Li, X.-B. Chen, Y.-H. Zou, S.-K. Guan,
694 E.-H. Han, In vitro corrosion resistance of a layer-by-layer assembled DNA coating on
695 magnesium alloy, Appl. Surf. Sci. 457 (2018) 49–58.
696 https://doi.org/10.1016/j.apsusc.2018.06.240.
697 [11] S.C. Cifuentes, E. Frutos, J.L. González-Carrasco, M. Muñoz, M. Multigner, J. Chao, R.
698 Benavente, M. Lieblich, Novel PLLA/magnesium composite for orthopedic applications: A
699 proof of concept, Mater. Lett. 74 (2012) 239–242.
700 https://doi.org/10.1016/j.matlet.2012.01.134.

[12] N. Argarate, B. Olalde, G. Atorrasagasti, J. Valero, S. Carolina Cifuentes, R. Benavente, M. Lieblich, J. Luis González-Carrasco, Biodegradable Bi-layered coating on polymeric orthopaedic implants for controlled release of drugs, Mater. Lett. 132 (2014) 193–195. https://doi.org/10.1016/j.matlet.2014.06.070.

[13] M. Salahshoor, Y. Guo, Biodegradable Orthopedic Magnesium-Calcium (MgCa) Alloys, Processing, and Corrosion Performance, Materials (Basel). 5 (2012) 135–155. https://doi.org/10.3390/ma5010135.

[14] S. Zhang, X. Zhang, C. Zhao, J. Li, Y. Song, C. Xie, H. Tao, Y. Zhang, Y. He, Y. Jiang, Research on an Mg–Zn alloy as a degradable biomaterial, Acta Biomater. 6 (2010) 626–640. https://doi.org/10.1016/j.actbio.2009.06.028.

[15] N.T. Kirkland, J. Lespagnol, N. Birbilis, M.P. Staiger, A survey of bio-corrosion rates of magnesium alloys, Corros. Sci. 52 (2010) 287–291. https://doi.org/10.1016/j.corsci.2009.09.033.

[16] M. Deng, L. Wang, D. Höche, S. V Lamaka, C. Wang, D. Snihirova, Y. Jin, Y. Zhang, M.L. Zheludkevich, Approaching “stainless magnesium” by Ca micro-alloying, Mater. Horizons. 8 (2021) 589–596. https://doi.org/10.1039/D0MH01380C.

[17] K. Hagihara, S. Shakudo, K. Fujii, T. Nakano, Degradation behavior of Ca–Mg–Zn intermetallic compounds for use as biodegradable implant materials, Mater. Sci. Eng. C. 44 (2014) 285–292. https://doi.org/10.1016/j.msec.2014.08.037.

[18] Y. Ding, C. Wen, P. Hodgson, Y. Li, Effects of alloying elements on the corrosion behavior and biocompatibility of biodegradable magnesium alloys: A review, J. Mater. Chem. B. 2 (2014) 1912–1933. https://doi.org/10.1039/c3tb21746a.

[19] F. Witte, J. Fischer, J. Nellesen, H.-A. Crostack, V. Kaese, A. Pisch, F. Beckmann, H. Windhagen, In vitro and in vivo corrosion measurements of magnesium alloys, Biomaterials. 27 (2006) 1013–1018. https://doi.org/10.1016/j.biomaterials.2005.07.037.

[20] F. Witte, N. Hort, C. Vogt, S. Cohen, K.U. Kainer, R. Willumeit, F. Feyerabend, Degradable

727 biomaterials based on magnesium corrosion, Curr. Opin. Solid State Mater. Sci. 12 (2008)
728 63–72. https://doi.org/10.1016/j.cossms.2009.04.001.
729 [21] M. Esmaily, J.E. Svensson, S. Fajardo, N. Birbilis, G.S. Frankel, S. Virtanen, R. Arrabal,
730 S. Thomas, L.G. Johansson, Fundamentals and advances in magnesium alloy corrosion,
731 Prog. Mater. Sci. 89 (2017) 92–193. https://doi.org/10.1016/j.pmatsci.2017.04.011.
732 [22] P. Salunke, V. Shanov, F. Witte, High purity biodegradable magnesium coating for implant
733 application, Mater. Sci. Eng. B. 176 (2011) 1711–1717.
734 https://doi.org/10.1016/j.mseb.2011.07.002.
735 [23] P. Nayak, Aluminum: Impacts and Disease, Environ. Res. 89 (2002) 101–115.
736 https://doi.org/10.1006/enrs.2002.4352.
737 [24] S.M. Mousavizadeh, Z. He, X. Wang, P. Shen, W. Wang, M.D. Gilchrist, N. Zhang, Surface
738 modification of WE43 magnesium alloy via alkali/stearic acid treatment for biodegradable
739 drug-eluting stent applications, Mater. Chem. Phys. 308 (2023) 128249.
740 https://doi.org/10.1016/j.matchemphys.2023.128249.
741 [25] H. Hornberger, S. Virtanen, A.R. Boccaccini, Biomedical coatings on magnesium alloys -
742 A review, Acta Biomater. 8 (2012) 2442–2455.
743 https://doi.org/10.1016/j.actbio.2012.04.012.
744 [26] M.A. Osipenko, J. Karczewski, M. Dominów, M. Prześniak-Welenc, I. V. Makarava, I.
745 Kurilo, D.S. Kharytonau, J. Ryl, Multisine impedimetric monitoring with an in-depth
746 distribution of relaxation times analysis of WE43 and AZ31 magnesium alloys corrosion,
747 Measurement. 222 (2023) 113683. https://doi.org/10.1016/j.measurement.2023.113683.
748 [27] B. Vaghefinazari, E. Wierzbicka, P. Visser, R. Posner, R. Arrabal, E. Matykina, M.
749 Mohedano, C. Blawert, M. Zheludkevich, S. Lamaka, Chromate-Free Corrosion Protection
750 Strategies for Magnesium Alloys—A Review: PART I—Pre-Treatment and Conversion
751 Coating, Materials (Basel). 15 (2022) 8676. https://doi.org/10.3390/ma15238676.
752 [28] X.B. Chen, N. Birbilis, T.B. Abbott, Review of Corrosion-Resistant Conversion Coatings

753 for Magnesium and Its Alloys, CORROSION. 67 (2011) 035005-1-035005–16.
754 https://doi.org/10.5006/1.3563639.
755 [29] M.A. Hafeez, A. Farooq, A. Zang, A. Saleem, K.M. Deen, Phosphate chemical conversion
756 coatings for magnesium alloys: a review, J. Coatings Technol. Res. 17 (2020) 827–849.
757 https://doi.org/10.1007/s11998-020-00335-2.
758 [30] Y. Su, Y. Guo, Z. Huang, Z. Zhang, G. Li, J. Lian, L. Ren, Preparation and corrosion
759 behaviors of calcium phosphate conversion coating on magnesium alloy, Surf. Coatings
760 Technol. 307 (2016) 99–108. https://doi.org/10.1016/j.surfcoat.2016.08.065.
761 [31] B. Liu, X. Zhang, G. Xiao, Y. Lu, Phosphate chemical conversion coatings on metallic
762 substrates for biomedical application: A review, Mater. Sci. Eng. C. 47 (2015) 97–104.
763 https://doi.org/10.1016/j.msec.2014.11.038.
764 [32] M.B. Kannan, Enhancing the performance of calcium phosphate coating on a magnesium
765 alloy for bioimplant applications, Mater. Lett. 76 (2012) 109–112.
766 https://doi.org/10.1016/j.matlet.2012.02.050.
767 [33] M.B. Kannan, O. Wallipa, Potentiostatic pulse-deposition of calcium phosphate on
768 magnesium alloy for temporary implant applications — An in vitro corrosion study, Mater.
769 Sci. Eng. C. 33 (2013) 675–679. https://doi.org/10.1016/j.msec.2012.10.017.
770 [34] S. Shadanbaz, G.J. Dias, Calcium phosphate coatings on magnesium alloys for biomedical
771 applications: A review, Acta Biomater. 8 (2012) 20–30.
772 https://doi.org/10.1016/j.actbio.2011.10.016.
773 [35] Y. Zhu, W. Liu, T. Ngai, Polymer coatings on magnesium-based implants for orthopedic
774 applications, J. Polym. Sci. 60 (2022) 32–51. https://doi.org/10.1002/pol.20210578.
775 [36] N. Scharnagl, C. Blawert, W. Dietzel, Corrosion protection of magnesium alloy AZ31 by
776 coating with poly(ether imides) (PEI), Surf. Coatings Technol. 203 (2009) 1423–1428.
777 https://doi.org/10.1016/j.surfcoat.2008.11.018.
778 [37] Q. Chen, S. Cabanas-Polo, O.-M. Goudouri, A.R. Boccaccini, Electrophoretic co-

779 deposition of polyvinyl alcohol (PVA) reinforced alginate–Bioglass® composite coating on
780 stainless steel: Mechanical properties and in-vitro bioactivity assessment, Mater. Sci. Eng.
781 C. 40 (2014) 55–64. https://doi.org/10.1016/j.msec.2014.03.019.
782 [38] A. Alabbasi, S. Liyanaarachchi, M.B. Kannan, Polylactic acid coating on a biodegradable
783 magnesium alloy: An in vitro degradation study by electrochemical impedance
784 spectroscopy, Thin Solid Films. 520 (2012) 6841–6844.
785 https://doi.org/10.1016/j.tsf.2012.07.090.
786 [39] D. Cuartas-Marulanda, L. Forero Cardozo, A. Restrepo-Osorio, P. Fernández-Morales,
787 Natural Coatings and Surface Modifications on Magnesium Alloys for Biomedical
788 Applications, Polymers (Basel). 14 (2022) 5297. https://doi.org/10.3390/polym14235297.
789 [40] P. Tong, Y. Sheng, R. Hou, M. Iqbal, L. Chen, J. Li, Recent progress on coatings of
790 biomedical magnesium alloy, Smart Mater. Med. 3 (2022) 104–116.
791 https://doi.org/10.1016/j.smaim.2021.12.007.
792 [41] L. Xu, A. Yamamoto, Characteristics and cytocompatibility of biodegradable polymer film
793 on magnesium by spin coating, Colloids Surfaces B Biointerfaces. 93 (2012) 67–74.
794 https://doi.org/10.1016/j.colsurfb.2011.12.009.
795 [42] K. Cai, X. Sui, Y. Hu, L. Zhao, M. Lai, Z. Luo, P. Liu, W. Yang, Fabrication of anticorrosive
796 multilayer onto magnesium alloy substrates via spin-assisted layer-by-layer technique,
797 Mater. Sci. Eng. C. 31 (2011) 1800–1808. https://doi.org/10.1016/j.msec.2011.08.012.
798 [43] R.N. Oosterbeek, C.K. Seal, J.-M. Seitz, M.M. Hyland, Polymer–bioceramic composite
799 coatings on magnesium for biomaterial applications, Surf. Coatings Technol. 236 (2013)
800 420–428. https://doi.org/10.1016/j.surfcoat.2013.10.029.
801 [44] L.-H. Li, T.S.N. Sankara Narayanan, Y.K. Kim, Y.-M. Kong, I.S. Park, T.S. Bae, M.H. Lee,
802 Deposition of microarc oxidation–polycaprolactone duplex coating to improve the
803 corrosion resistance of magnesium for biodegradable implants, Thin Solid Films. 562
804 (2014) 561–567. https://doi.org/10.1016/j.tsf.2014.04.004.

[45] I. Johnson, K. Akari, H. Liu, Nanostructured hydroxyapatite/poly(lactic- co -glycolic acid) composite coating for controlling magnesium degradation in simulated body fluid, Nanotechnology. 24 (2013) 375103. https://doi.org/10.1088/0957-4484/24/37/375103.

[46] A.R. Boccaccini, M. Erol, W.J. Stark, D. Mohn, Z. Hong, J.F. Mano, Polymer/bioactive glass nanocomposites for biomedical applications: A review, Compos. Sci. Technol. 70 (2010) 1764–1776. https://doi.org/10.1016/j.compscitech.2010.06.002.

[47] M. Rahman, Y. Li, C. Wen, Realization and characterization of double-layer Ca-P coating on WE43 Mg alloy for biomedical applications, Surf. Coatings Technol. 398 (2020) 126091. https://doi.org/10.1016/j.surfcoat.2020.126091.

[48] S. V. Lamaka, B. Vaghefinazari, D. Mei, R.P. Petrauskas, D. Höche, M.L. Zheludkevich, Comprehensive screening of Mg corrosion inhibitors, Corros. Sci. 128 (2017) 224–240. https://doi.org/10.1016/j.corsci.2017.07.011.

[49] E. Wierzbicka, B. Vaghefinazari, M. Mohedano, P. Visser, R. Posner, C. Blawert, M. Zheludkevich, S. Lamaka, E. Matykina, R. Arrabal, Chromate-Free Corrosion Protection Strategies for Magnesium Alloys—A Review: Part II—PEO and Anodizing, Materials (Basel). 15 (2022) 8515. https://doi.org/10.3390/ma15238515.

[50] P. Nowak, M. Mosiałek, D.S. Kharitonov, J. Adamiec, A. Turowska, Effect of TIG Welding and Rare Earth Elements Alloying on Corrosion Resistance of Magnesium Alloys, J. Electrochem. Soc. 167 (2020) 131504. https://doi.org/10.1149/1945-7111/abb97e.

[51] K.Z. Chong, T.S. Shih, Conversion-coating treatment for magnesium alloys by a permanganate–phosphate solution, Mater. Chem. Phys. 80 (2003) 191–200. https://doi.org/10.1016/S0254-0584(02)00481-9.

[52] V.S. Saji, Review of rare-earth-based conversion coatings for magnesium and its alloys, J. Mater. Res. Technol. 8 (2019) 5012–5035. https://doi.org/10.1016/j.jmrt.2019.08.013.

[53] D. Mei, S. V. Lamaka, X. Lu, M.L. Zheludkevich, Selecting medium for corrosion testing of bioabsorbable magnesium and other metals – A critical review, Corros. Sci. 171 (2020)

108722. https://doi.org/10.1016/j.corsci.2020.108722.

[54] S. V. Lamaka, J. Gonzalez, D. Mei, F. Feyerabend, R. Willumeit-Römer, M.L. Zheludkevich, Local pH and Its Evolution Near Mg Alloy Surfaces Exposed to Simulated Body Fluids, Adv. Mater. Interfaces. 5 (2018) 1800169. https://doi.org/10.1002/admi.201800169.

[55] M.A. Osipenko, D.S. Kharytonau, A.A. Kasach, J. Ryl, J. Adamiec, I.I. Kurilo, Inhibitive Effect of Sodium Molybdate on Corrosion of AZ31 Magnesium Alloy in Chloride Solutions, Electrochim. Acta. 414 (2022) 140175. https://doi.org/10.1016/j.electacta.2022.140175.

[56] H.S. Jiang, M.Y. Zheng, X.G. Qiao, K. Wu, Q.Y. Peng, S.H. Yang, Y.H. Yuan, J.H. Luo, Microstructure and mechanical properties of WE43 magnesium alloy fabricated by direct-chill casting, Mater. Sci. Eng. A. 684 (2017) 158–164. https://doi.org/10.1016/j.msea.2016.11.009.

[57] D.S. Kharitonov, M. Zimowska, J. Ryl, A. Zieliński, M.A. Osipenko, J. Adamiec, A. Wrzesińska, P.M. Claesson, I.I. Kurilo, Aqueous molybdate provides effective corrosion inhibition of WE43 magnesium alloy in sodium chloride solutions, Corros. Sci. 190 (2021) 109664. https://doi.org/10.1016/j.corsci.2021.109664.

[58] L. Xu, C. Liu, Y. Wan, X. Wang, H. Xiao, Effects of heat treatments on microstructures and mechanical properties of Mg–4Y–2.5Nd–0.7Zr alloy, Mater. Sci. Eng. A. 558 (2012) 1–6. https://doi.org/10.1016/j.msea.2012.06.085.

[59] M. Esmaily, Z. Zeng, A.N. Mortazavi, A. Gullino, S. Choudhary, T. Derra, F. Benn, F. D'Elia, M. Müther, S. Thomas, A. Huang, A. Allanore, A. Kopp, N. Birbilis, A detailed microstructural and corrosion analysis of magnesium alloy WE43 manufactured by selective laser melting, Addit. Manuf. 35 (2020) 101321. https://doi.org/10.1016/j.addma.2020.101321.

[60] N.A. Zumdick, L. Jauer, L.C. Kersting, T.N. Kutz, J.H. Schleifenbaum, D. Zander, Additive

manufactured WE43 magnesium: A comparative study of the microstructure and mechanical properties with those of powder extruded and as-cast WE43, Mater. Charact. 147 (2019) 384–397. https://doi.org/10.1016/j.matchar.2018.11.011.

[61] J. Xie, J. Zhang, Z. You, S. Liu, K. Guan, R. Wu, J. Wang, J. Feng, Towards developing Mg alloys with simultaneously improved strength and corrosion resistance via RE alloying, J. Magnes. Alloy. 9 (2021) 41–56. https://doi.org/10.1016/j.jma.2020.08.016.

[62] S. Nanaki, P. Barmpalexis, A. Iatrou, E. Christodoulou, M. Kostoglou, D. Bikiaris, Risperidone Controlled Release Microspheres Based on Poly(Lactic Acid)-Poly(Propylene Adipate) Novel Polymer Blends Appropriate for Long Acting Injectable Formulations, Pharmaceutics. 10 (2018) 130. https://doi.org/10.3390/pharmaceutics10030130.

[63] X. Guo, L. Yu, L. Chen, H. Zhang, L. Peng, X. Guo, W. Ding, Organoamine-assisted biomimetic synthesis of faceted hexagonal hydroxyapatite nanotubes with prominent stimulation activity for osteoblast proliferation, J. Mater. Chem. B. 2 (2014) 1760–1763. https://doi.org/10.1039/C3TB21652G.

[64] H. Zhou, J. Li, J. Li, Q. Ruan, W. Jin, Z. Yu, W. Li, P.K. Chu, Calcium phosphate coating on biomedical WE43 magnesium alloy pretreated with a magnesium phosphate layer for corrosion protection, Surf. Coatings Technol. 401 (2020) 126248. https://doi.org/10.1016/j.surfcoat.2020.126248.

[65] C. Ke, M.-S. Song, R.-C. Zeng, Y. Qiu, Y. Zhang, R.-F. Zhang, R.-L. Liu, I. Cole, N. Birbilis, X.-B. Chen, Interfacial study of the formation mechanism of corrosion resistant strontium phosphate coatings upon Mg-3Al-4.3Ca-0.1Mn, Corros. Sci. 151 (2019) 143–153. https://doi.org/10.1016/j.corsci.2019.02.024.

[66] K. Dong, Y. Song, D. Shan, E.-H. Han, An optimization of pretreatment for the phosphate conversion film on WE43 magnesium alloy, Mater. Corros. 69 (2018) 481–491. https://doi.org/10.1002/maco.201709742.

[67] G. Kühl, W.H. Nebergall, Hydrogenphosphat- und Carbonatapatite, Zeitschrift Für Phys.

Chemier Anorg. Und Allg. Chemie. 324 (1963) 313–320. https://doi.org/10.1002/zaac.19633240513.

[68] Z. Zhu, Y. Bian, X. Zhang, R. Zeng, B. Yang, Study of Crystallinity and Conformation of Poly(lactic acid) by Terahertz Spectroscopy, Anal. Chem. 94 (2022) 11104–11111. https://doi.org/10.1021/acs.analchem.2c02652.

[69] V.S.G. Silverajah, N.A. Ibrahim, N. Zainuddin, W.M.Z.W. Yunus, H.A. Hassan, Mechanical, Thermal and Morphological Properties of Poly(lactic acid)/Epoxidized Palm Olein Blend, Molecules. 17 (2012) 11729–11747. https://doi.org/10.3390/molecules171011729.

[70] D. Liu, L. Mao, H. Wang, Preparation of uniform newberyite crystal in nonaqueous system, Mater. Lett. 240 (2019) 169–171. https://doi.org/10.1016/j.matlet.2019.01.016.

[71] K.H. Park, S.-J. Kim, W.-Y. Lee, H.-J. Song, Y.-J. Park, Hydrothermal fabrication and characterization of calcium phosphate anhydrous/chitosan composites, Ceram. Int. 43 (2017) 2786–2790. https://doi.org/10.1016/j.ceramint.2016.11.112.

[72] D.H. Butler, R. Shahack-Gross, Formation of Biphasic Hydroxylapatite-Beta Magnesium Tricalcium Phosphate in Heat Treated Salmonid Vertebrae, Sci. Rep. 7 (2017) 3610. https://doi.org/10.1038/s41598-017-03737-2.

[73] L. Spevak, C.R. Flach, T. Hunter, R. Mendelsohn, A. Boskey, Fourier Transform Infrared Spectroscopic Imaging Parameters Describing Acid Phosphate Substitution in Biologic Hydroxyapatite, Calcif. Tissue Int. 92 (2013) 418–428. https://doi.org/10.1007/s00223-013-9695-9.

[74] X. Chen, X. Wang, D. Fang, A review on C1s XPS-spectra for some kinds of carbon materials, Fullerenes, Nanotub. Carbon Nanostructures. 28 (2020) 1048–1058. https://doi.org/10.1080/1536383X.2020.1794851.

[75] H. Fang, C. Wang, S. Zhou, G. Li, Y. Tian, T. Suga, Exploration of the enhanced performances for silk fibroin/sodium alginate composite coatings on biodegradable

Mg−Zn−Ca alloy, J. Magnes. Alloy. 9 (2021) 1578–1594. https://doi.org/10.1016/j.jma.2020.08.017.

[76] G. Sourkouni, C. Kalogirou, P. Moritz, A. Gödde, P.K. Pandis, O. Höfft, S. Vouyiouka, A.A. Zorpas, C. Argirusis, Study on the influence of advanced treatment processes on the surface properties of polylactic acid for a bio-based circular economy for plastics, Ultrason. Sonochem. 76 (2021) 105627. https://doi.org/10.1016/j.ultsonch.2021.105627.

[77] K. NAGAKANE, Y. YOSHIDA, I. HIRATA, R. FUKUDA, Y. NAKAYAMA, K. SHIRAI, T. OGAWA, K. SUZUKI, B. VAN MEERBEEK, M. OKAZAKI, Analysis of Chemical Interaction of 4-MET with Hydroxyapatite Using XPS, Dent. Mater. J. 25 (2006) 645–649. https://doi.org/10.4012/dmj.25.645.

[78] C. Kalogirou, O. Höfft, A. Gödde, N. Papadimitriou, P.K. Pandis, C. Argirusis, G. Sourkouni, Assessing the Time Dependence of AOPs on the Surface Properties of Polylactic Acid, J. Polym. Environ. 31 (2023) 345–357. https://doi.org/10.1007/s10924-022-02608-w.

[79] F.P. Gokdemir Choi, H. Moeini Alishah, S. Bozar, C. Kahveci, M. Canturk Rodop, S. Gunes, First demonstration of lithium, cobalt and magnesium introduced nickel oxide hole transporters for inverted methylammonium lead triiodide based perovskite solar cells, Sol. Energy. 215 (2021) 434–442. https://doi.org/10.1016/j.solener.2020.12.068.

[80] I. Puigdomenech, Hydra/Medusa Chemical Equilibrium Database and Plotting Software, (2010).

[81] L. C. CHOW, Next generation calcium phosphate-based biomaterials, Dent. Mater. J. 28 (2009) 1–10. https://doi.org/10.4012/dmj.28.1.

[82] Y. Song, D. Shan, R. Chen, F. Zhang, E.-H. Han, A novel phosphate conversion film on Mg–8.8Li alloy, Surf. Coatings Technol. 203 (2009) 1107–1113. https://doi.org/10.1016/j.surfcoat.2008.10.004.

[83] A.D. King, N. Birbilis, J.R. Scully, Accurate electrochemical measurement of magnesium

corrosion rates; A combined impedance, mass-loss and hydrogen collection study, Electrochim. Acta. 121 (2014) 394–406. https://doi.org/10.1016/j.electacta.2013.12.124.

[84] D.S. Kharitonov, C. Ornek, P.M. Claesson, J. Sommertune, I.M. Zharskii, I.I. Kurilo, J. Pan, Corrosion Inhibition of Aluminum Alloy AA6063-T5 by Vanadates : Microstructure Characterization and Corrosion Analysis, J. Electrochem. Soc. 165 (2018) C116–C126. https://doi.org/10.1149/2.0341803jes.

[85] L. Wang, D. Snihirova, M.D. Havigh, M. Deng, S. V. Lamaka, H. Terryn, M.L. Zheludkevich, Non-stationarity in electrochemical impedance measurement of Mg-based materials in aqueous media, Electrochim. Acta. 468 (2023) 143140. https://doi.org/10.1016/j.electacta.2023.143140.

[86] G. Song, A. Atrens, Understanding Magnesium Corrosion—A Framework for Improved Alloy Performance, Adv. Eng. Mater. 5 (2003) 837–858. https://doi.org/10.1002/adem.200310405.

[87] W. Zai, Y. Su, H.C. Man, J. Lian, G. Li, Effect of pH value and preparation temperature on the formation of magnesium phosphate conversion coatings on AZ31 magnesium alloy, Appl. Surf. Sci. 492 (2019) 314–327. https://doi.org/10.1016/j.apsusc.2019.05.309.

[88] W. Zhou, D. Shan, E.-H. Han, W. Ke, Structure and formation mechanism of phosphate conversion coating on die-cast AZ91D magnesium alloy, Corros. Sci. 50 (2008) 329–337. https://doi.org/10.1016/j.corsci.2007.08.007.

[89] Y. He, Y. Inoue, Novel FTIR method for determining the crystallinity of poly(?-caprolactone), Polym. Int. 49 (2000) 623–626. https://doi.org/10.1002/1097-0126(200006)49:6<623::AID-PI435>3.0.CO;2-8.

[90] M. Partini, R. Pantani, Determination of crystallinity of an aliphatic polyester by FTIR spectroscopy, Polym. Bull. 59 (2007) 403–412. https://doi.org/10.1007/s00289-007-0782-9.

[91] M.A. Osipenko, A.A. Kasach, J. Adamiec, M. Zimowska, I.I. Kurilo, D.S. Kharytonau,

Corrosion inhibition of magnesium alloy AZ31 in chloride-containing solutions by aqueous permanganate, J. Solid State Electrochem. (2023). https://doi.org/10.1007/s10008-023-05472-3.

[92] D. Höche, C. Blawert, S. V. Lamaka, N. Scharnagl, C. Mendis, M.L. Zheludkevich, The effect of iron re-deposition on the corrosion of impurity-containing magnesium, Phys. Chem. Chem. Phys. 18 (2016) 1279–1291. https://doi.org/10.1039/C5CP05577F.

[93] M. Taheri, J.R. Kish, N. Birbilis, M. Danaie, E.A. McNally, J.R. McDermid, Towards a Physical Description for the Origin of Enhanced Catalytic Activity of Corroding Magnesium Surfaces, Electrochim. Acta. 116 (2014) 396–403. https://doi.org/10.1016/j.electacta.2013.11.086.

[94] D. Lysne, S. Thomas, M.F. Hurley, N. Birbilis, On the Fe Enrichment during Anodic Polarization of Mg and Its Impact on Hydrogen Evolution, J. Electrochem. Soc. 162 (2015) C396–C402. https://doi.org/10.1149/2.0251508jes.